Anderson Localization of Walking Droplets

Abel J. Abraham,[1] Stepan Malkov,[1] Frane A. Ljubetic,[1] Matthew Durey,[2] and Pedro J. Sáenz[1,*]
[1]Department of Mathematics, University of North Carolina, Chapel Hill, North Carolina 27599, USA
[2]School of Mathematics and Statistics, University of Glasgow, University Place, Glasgow, G12 8QQ, United Kingdom

(Received 10 December 2023; revised 28 May 2024; accepted 29 July 2024; published 17 September 2024)

Understanding the ability of particles to maneuver through disordered environments is a central problem in innumerable settings, from active matter and biology to electronics. Macroscopic particles ultimately exhibit diffusive motion when their energy exceeds the characteristic potential barrier of the random landscape. In stark contrast, wave-particle duality causes electrons in disordered media to come to rest even when the potential is weak—a remarkable phenomenon known as Anderson localization. Here, we present a hydrodynamic active system with wave-particle features, a millimetric droplet self-guided by its own wave field over a submerged random topography, whose dynamics exhibits localized statistics analogous to those of electronic systems. Consideration of an ensemble of particle trajectories reveals a suppression of diffusion when the guiding wave field extends over the disordered topography. We rationalize mechanistically the emergent statistics by virtue of the wave-mediated resonant coupling between the droplet and topography, which produces an attractive wave potential about the localization region. This hydrodynamic analog, which demonstrates how a classical particle may localize like a wave, suggests new directions for future research in various areas, including active matter, wave localization, many-body localization, and topological matter.

DOI: 10.1103/PhysRevX.14.031047 Subject Areas: Fluid Dynamics, Soft Matter

I. INTRODUCTION

Disorder is omnipresent in nature. Investigating the motion of particles in heterogeneous media has, thus, always captivated scientists across disciplines, yielding an ever-growing list of transformative breakthroughs. Modern examples are abundant in the fields of active matter [1,2], including systems of flocking colloids cruising over random obstacles [3] or microbial dispersion in porous media [4], and condensed matter, including states of matter insensitive to defects [5] or particlelike magnetic excitations in quenched disorder [6] that show promise for the development of spintronics [7,8]. Classic examples comprise the erratic motion of pollen grains caused by the molecules of their enveloping fluid [9] and the turbulent transport of plankton and other marine ecosystems [10]. Of particular interest, for both fundamental and practical reasons, is the comparative study of classical and subatomic particle dynamics in random landscapes. When macroscopic particles, such as billiard balls, move with high kinetic energy across a weak disordered background, they are deflected by small random forces that eventually cause their motion to become diffusive in two (or higher) dimensions [2]. Subatomic particles display a fundamentally different behavior. An electron may spontaneously come to a halt, or "localize," over a relatively weak random potential for a sufficient degree of disorder [11,12]; this phenomenon, Anderson localization, has reshaped condensed matter physics [13–15]. Here, we demonstrate that macroscopic "walking droplets" [16] [Fig. 1(a)], which propel along the surface of a vibrating fluid bath guided by their own self-excited wave field, may exhibit analogous localization.

Anderson localization results from the wavelike behavior of electrons [13–15]. Hence, significant research efforts have pursued demonstrating the universality [14] of wave localization across diverse systems, including matter waves [18–20], microwaves and light waves [21–25], ultrasound [26], and water waves [27,28]. Today, Anderson localization is thus widely regarded as a purely classical wave phenomenon [29]. Inspired by their quantum counterparts, however, our interest is to investigate whether classical *particles* may localize like waves.

To test this hypothesis, we consider the wave-mediated spontaneous motion of a bouncing droplet on the surface of a vibrating fluid bath [Fig. 1(a)] subjected to vertical forcing acceleration $\Gamma(t) = \gamma\cos(2\pi f t)$, where γ is the maximum acceleration, f the oscillation frequency, and t time. Despite being macroscopic objects, these walking

*Contact author: saenz@unc.edu

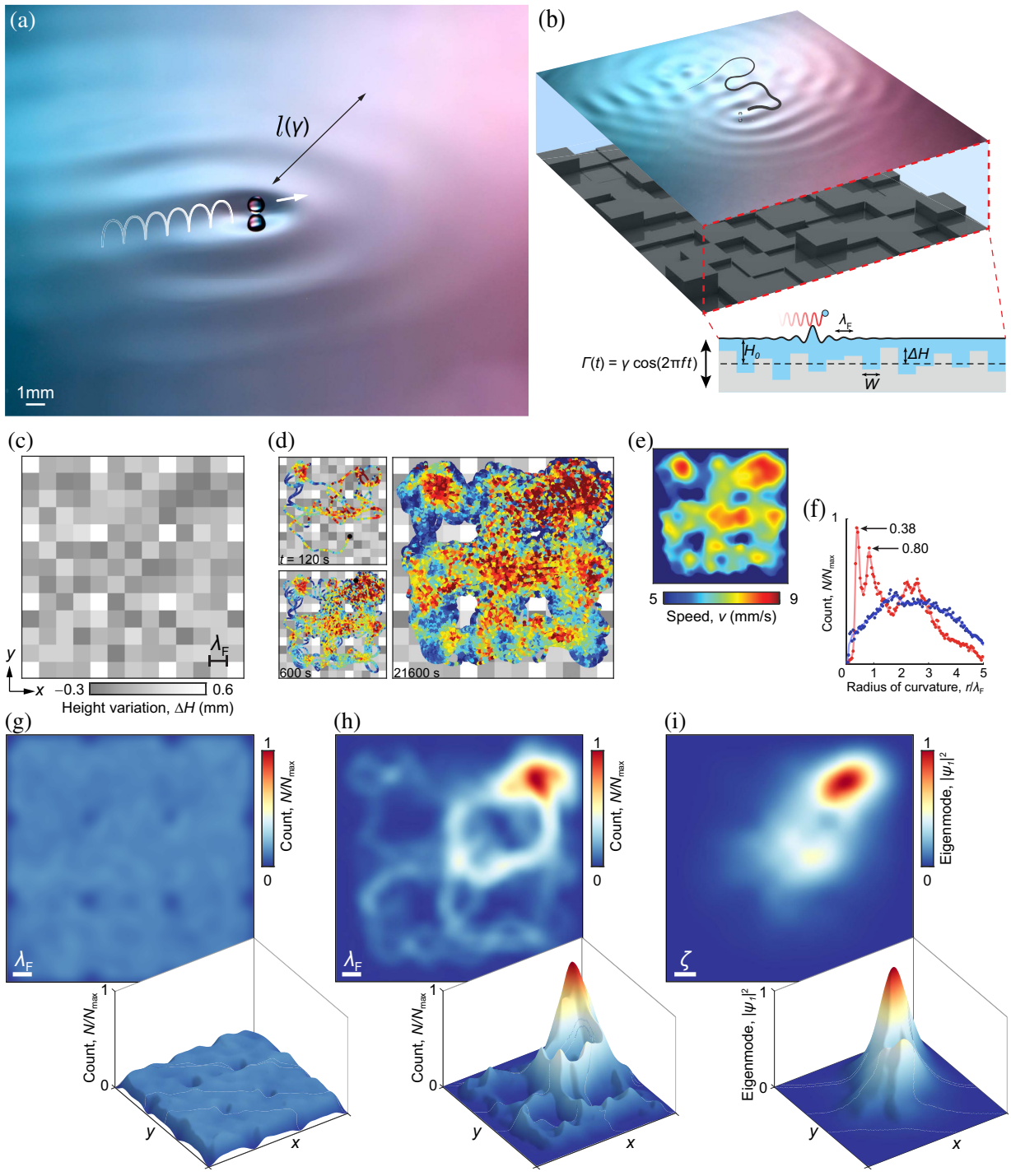

FIG. 1. Localization of walking droplets over submerged random topographies. (a) Oblique view of a walking droplet self-propelled by its own guiding wave field. (b) In our experiments, the droplet moves erratically (Supplemental Material Video 1 [17]) due to the nonlocal influence of a submerged disordered topography (not to scale vertically) composed of square tiles, each of width $W = 5.25$ mm (matching the Faraday wavelength λ_F) and random height (uniform distribution in the interval $\pm\Delta H$) around a base depth $H_0 = 1.85$ mm. (c) Random realization of the submerged topography used in our experiments. (d) At high memory ($\gamma/\gamma_F = 99.8\%$), the walker trajectory (colored according to the instantaneous speed) reveals a chaotic exploration of the domain. (e) After 6 h, the average local speed shows regions of higher and lower speeds roughly corresponding to deeper and shallower areas, respectively. (f) Comparison of the radius of curvature of the trajectory for our walker (red) and a "waveless" particle (blue) in the same random potential (each normalized by the overall maximum N_{max}). The walker moves at an average speed $v_0 = 7.3$ mm/s, turning along preferred radii of curvature $r/\lambda_F \sim 0.38$ and 0.80. The position histogram for the waveless particle is uniform (g). Notably, the walker position histogram exhibits a localization region (h), which bears a strong resemblance to the first eigenmode of Schrödinger's equation for the same potential in the weak regime (i).

droplets display dual wave-particle behaviors reminiscent of those arising in quantum systems [30]. As the forcing acceleration is increased, the droplet begins to bounce at half of the driving frequency, thus achieving resonance with the most unstable wave mode of the bath [31,32]. At each bounce, the droplet excites decaying circular waves, with wavelength λ_F, whose influence on the droplet dynamics increases with the forcing acceleration [33]. When the driving exceeds a critical walking threshold, $\gamma > \gamma_w$, vertical bouncing becomes unstable and the droplet starts to land on the slope of the wave field generated at previous impacts. The droplet, thus, experiences a wave-induced horizontal force $\mathbf{F}(\boldsymbol{x}, t) \propto -\nabla\eta|_{\boldsymbol{x}=\boldsymbol{x}_p}$, proportional to the slope of the underlying wave field, $\eta(\boldsymbol{x}, t)$, at the particle's location, $\boldsymbol{x}_p(t)$ [31,33]. Acting as self-propelled wave sources [30], walking droplets, or "walkers," thus move along straight paths at constant speeds on the surface of a homogeneous bath [31].

To investigate the walker motion in disordered media, we leverage variable bottom topography to subject the droplet to spatially varying potentials [34–36]. In our experiments, the bath's bottom profile is composed of square tiles, each with a random height around a base depth $H_0 = 1.85$ mm drawn from the uniform distribution in the interval $\Delta H = \pm 0.3$ mm [Fig. 1(b)]. Hence, the fluid depth is $H(\boldsymbol{x}) = H_0 - \Delta H(\boldsymbol{x})$. A wave damper surrounding the heterogeneous bottom prevents the droplet from escaping the disordered domain (Appendix A). The tile width $W = 5.25$ mm is selected to match the characteristic Faraday wavelength λ_F, dictated by the capillary-gravity dispersion relation [37] for the base depth H_0. Notably, the depth variations in our experiments have a negligible influence on λ_F. The droplet, with radius $R = 0.368$ mm, and fluid bath are composed of the same 20 cSt silicon oil with kinematic viscosity ν, density ρ, and surface tension σ. The bath is vibrated with an electromagnetic shaker with oscillation frequency $f = 70$ Hz (Fig. 5). The experimental topography [Fig. 1(c)] includes regularly spaced pillars, $\Delta H = 0.6$ mm, to facilitate data acquisition, which play no significant role in the localization (Appendix D). Equipped with this strategy to tune spatial disorder in the walker system, we investigated the droplet's motion over submerged random topographies.

The quantumlike effects of the walker system emerge when the droplet motion is strongly influenced by the underlying wave field [30], which is characterized by a spatial extent l and a decay, or "memory," time T_M [33,38]. Both of these spatiotemporal features increase as the forcing acceleration approaches the Faraday threshold $\gamma_F = 3.775g$ ($g = 9.81\text{m/s}^2$), at which the entire bath surface becomes unstable to standing waves [37]. We, thus, focus on the walker's statistical behavior in the high-memory regime $\gamma/\gamma_F = 99.8\%$, when the waves are long-lived, $T_M \sim 26$ s, and span a large area of the bath, $l \sim 7\lambda_F$. No waves exist in the absence of the droplet ($\gamma < \gamma_F$). To achieve statistical significance, we record the droplet motion for 6 h, which corresponds to 756 000 bounces and roughly 2300 domain crossings. The data are acquired in 20 min intervals to maintain the prescribed memory (Appendix A).

II. LOCALIZED STATISTICS

The walking droplet moves erratically above the heterogeneous bottom topography due to deformations in the wave field produced by the disordered features below the bath surface [Fig. 1(d) and Supplemental Material Video 1 [17]]. The chaotic trajectory is characterized by random speed fluctuations that typically occur at a length scale shorter than that of the underlying topography, W, thus evidencing the presence of wave-mediated forces produced by distant submerged features. The spatially averaged speed map reveals areas of higher and lower speeds roughly corresponding to deeper and shallower regions, respectively [Fig. 1(e)], indicating a depth-dependent speed envelope superimposed on the high-frequency speed fluctuations.

To contextualize the distinct walker behavior, we compare their statistics to those arising from a "waveless" particle, that evolves classically according to $m\ddot{\boldsymbol{x}}_p(t) = -\nabla V(\boldsymbol{x}_p)$, and a quantum particle governed by Schrödinger's equation, $i\hbar\Psi_t(\boldsymbol{x}, t) = -\hbar^2\nabla^2\Psi/2m + V(\boldsymbol{x})\Psi$, where m is the particle mass and Ψ the wave function. The particles are subject to a random potential of the same form as the experimental bottom topography, $V(\boldsymbol{x}) = -\kappa[H(\boldsymbol{x}) - \max H(\boldsymbol{x})]$, up to a rescaling constant κ. Anderson localization is unique, because the particles become effectively trapped when the potential is sufficiently disordered but weak relative to the particle's kinetic energy [39] (Appendix C). In our simulations, we thus adjust the constant κ and the initial particle energy to ensure that the total energy is larger than the background potential. For the waveless particles, we also match the average speed to that in our experiments. The effect of the wave damper along the border of the heterogeneous region is modeled through a confining potential for the waveless particle and Dirichlet boundary conditions in the quantum simulations (Appendixes D and C, respectively).

The emergent speed statistics for the walker and waveless particle are similar [Figs. 9 and 10(a)]. However, the distribution of the radius of curvature of the walker trajectory reveals a lack of tight turns and, instead, significant peaks at $r/\lambda_F \sim 0.38$ and 0.80 [Fig. 1(f)], roughly corresponding to the preferred radii observed in experiments involving walkers forced along curved paths [40]. The trajectory of the waveless particle exhibits more violent velocity reversals and wider turns [Figs. 1(f) and 9(a)]. The walker, thus, turns along more restricted trajectories due to the influence of the pilot wave field, which sets a kinematic constraint on the preferred path curvature [41].

A much more profound difference is observed when comparing the spatial distributions of the particles. The position histogram for the waveless particle is relatively

homogeneous [Fig. 1(g)]; the particle, thus, explores the domain uniformly. In contrast, the walker's position histogram features a prominent peak, or "localization" region [Fig. 1(h)], where the walker returns more frequently and spends more time. Notably, the observed walker localization bears a strong resemblance to the first eigenmode in the Anderson regime for a quantum particle in the same random potential [Fig. 1(i); see Appendix C].

To further probe the mechanisms underpinning the walker localization, we complement our experiments with simulations of walking droplets with a quasipotential fluid model [42], for which the bath surface elevation evolves according to

$$u_t = -G(t)\eta + \frac{\sigma}{\rho}\Delta\eta + 2\nu\Delta u - \frac{P}{\rho},$$
$$\eta_t = \mathcal{L}u + 2\nu\Delta\eta, \tag{1}$$

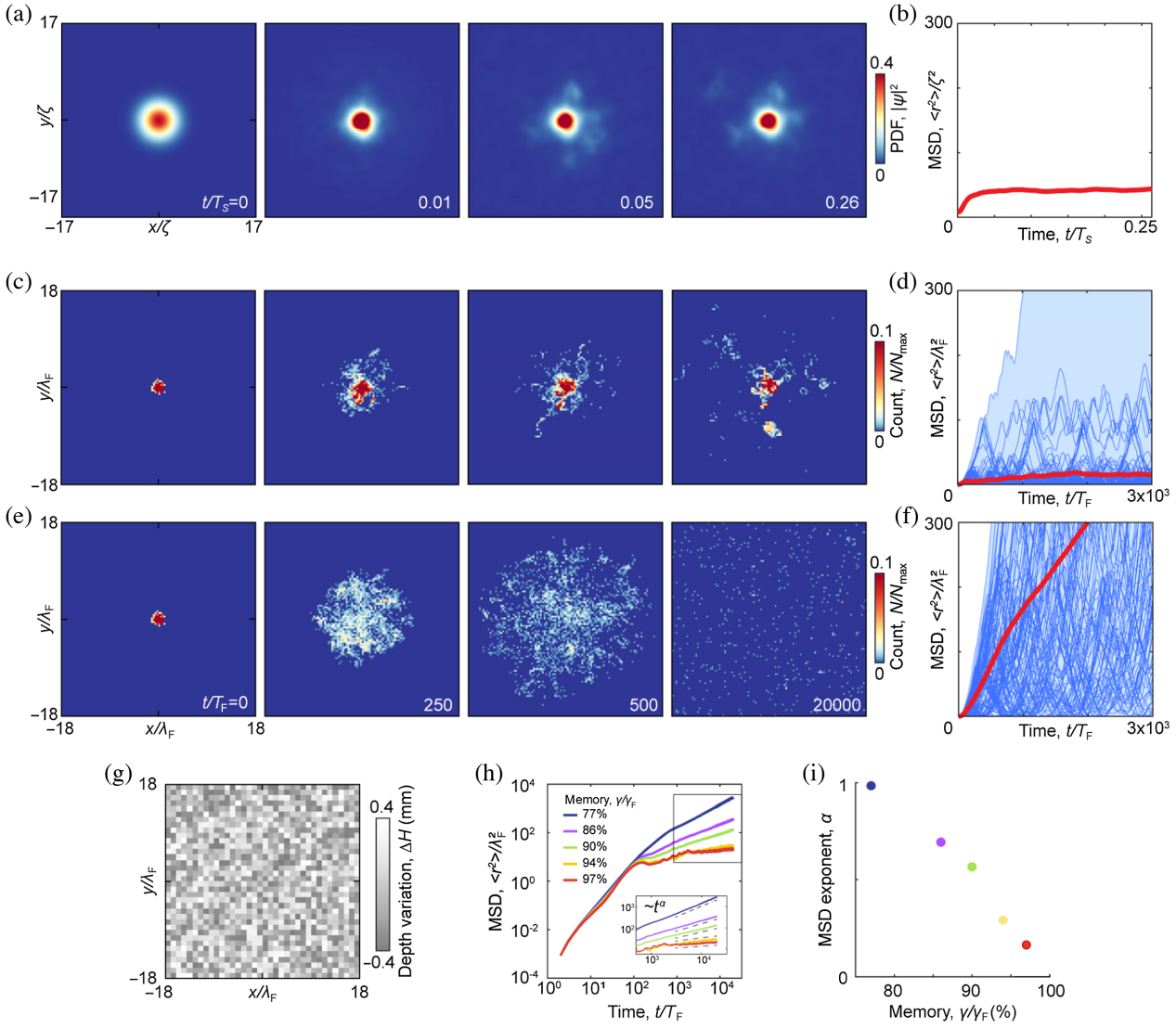

FIG. 2. Absence of diffusion in the walker system. (a) Anderson localization is observed in the temporal evolution of a quantum wave packet, $|\Psi|^2$, over a weak random potential. The probability-density function becomes localized due to the disorder; the distribution's mean-squared displacement (MSD) saturates in the long-time limit (b). (c),(d) A similar absence of diffusion is observed in simulations of an ensemble of walking droplets at high memory, $\gamma/\gamma_F = 97\%$, which become localized due to the influence of their wave field. (e),(f) At low memory, $\gamma/\gamma_F = 77\%$, when the walker's wave field is smaller and shorter-lived, the droplets move freely. (g) Sample of random topography. (h) Long-time evolution of the MSD shown in (d) and (f) and from other values of memory. (i) Dependence on memory of the MSD's temporal exponent, showing a gradual decrease as the memory is increased. The average walker speed is $v_0 = 5.1$ mm/s in all cases. In (a) and (b), we average over 20 random potentials. Space and time are normalized according to the correlation length ζ and $T_S = mL^2/\hbar$, respectively (Appendix C). In (c)–(j), we average over eight random topographies with $H_0 = 1.45$ mm and 400 walker trajectories for each realization. Time is normalized by the Faraday period, $T_F = 2/f$ (Appendix D). See Supplemental Material Video 2 [17] for video animations of (a), (c), and (e).

where $u(\boldsymbol{x},t)$ is the linearized free-surface velocity potential, $G(t)$ the effective gravitational acceleration, and P the pressure exerted on the free surface during each bounce. The operator $\mathcal{L}(\boldsymbol{x}) = -\nabla\cdot b(\boldsymbol{x})\nabla$ captures the influence of variable bottom topography by adjusting the local wave speed through an effective depth $b(\boldsymbol{x})$. The droplet position evolves according to $m\ddot{\boldsymbol{x}}_p(t) + D(t)\dot{\boldsymbol{x}}_p(t) = -F(t)\nabla\eta(\boldsymbol{x}_p,t)$, where $D(t)$ is the viscous dissipation and $F(t)$ the interaction force (Appendix B). Armed with this walker model, which provides good agreement with our experiments [Figs. 9(b) and 9(c)], we examine next whether the walker localized statistics suppress diffusion as in the quantum system.

III. SUPPRESSION OF DIFFUSION

In Anderson localization, the evolution of a quantum particle, represented by the probability density function (PDF) $|\Psi|^2$, spontaneously comes to a halt over a sufficiently random potential even though the particle's energy is larger than the background potential [Fig. 2(a)]. After an initial ballistic phase caused by short-time scattering [39], the PDF's mean-squared displacement (MSD) $\langle r^2(t)\rangle = \iint_\Omega |\Psi|^2|\boldsymbol{x}|^2 dS$ saturates in time [Fig. 2(b) and Appendix C]. To test whether a similar suppression of diffusion occurs in our hydrodynamic system, we perform walker simulations with eight random realizations of the topography over domains larger than those feasible in experiments [Fig. 2(g)]. Each realization is explored by 400 walkers for 2×10^4 Faraday periods, $T_F = 2/f$. We tune the base depth $H_0 = 1.45$ mm and particle's average speed $v_0 = 5.2$ mm/s (Appendix D). Indeed, at high memory, $\gamma/\gamma_F = 97\%$, when wavelike behavior of walking droplets is most prominent [30], we observe that the position histogram remains localized and effectively froze [Fig. 2(c)]. Similarly, the MSD of the particle ensemble, $\langle r^2(t)\rangle = (1/N)\sum_{i=1}^{N}|\boldsymbol{x}_{p_i}|^2$, saturates in the long-time limit, revealing an absence of diffusion in the walker system [Fig. 2(d)].

To demonstrate that the droplet localization is correlated to the spatiotemporal attributes of its pilot wave, we also

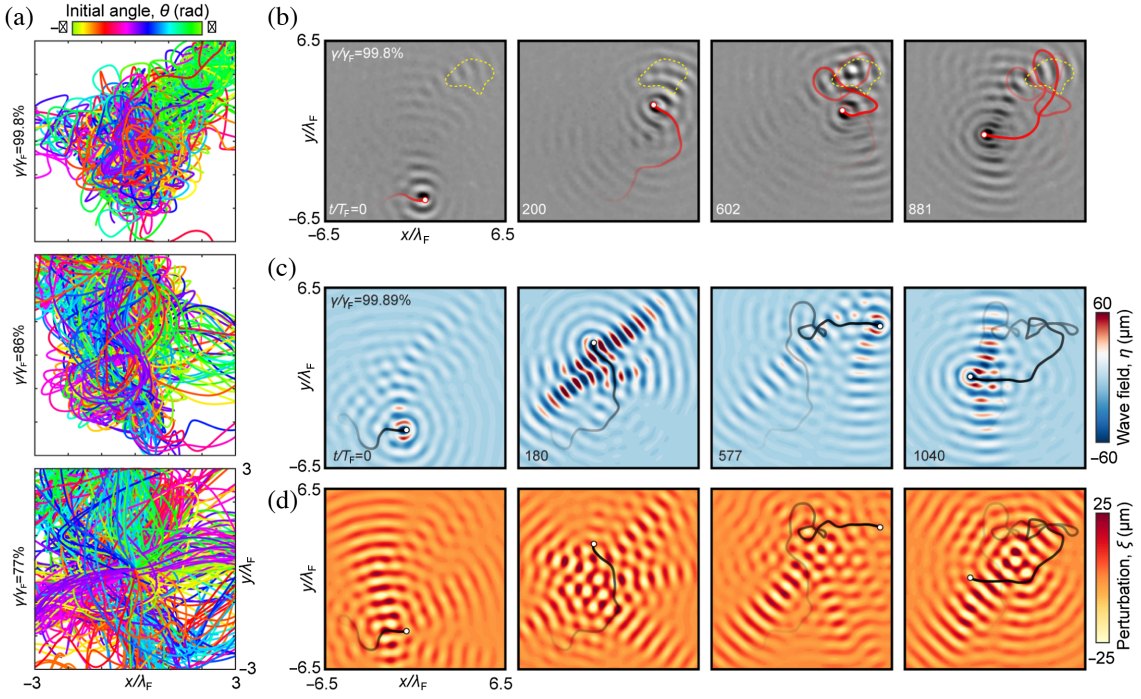

FIG. 3. Spatiotemporal nonlocal interactions cause the walker localization. (a) The initial spreading of the simulations described in Figs. 2(c)–2(i) reveal that the droplet trajectories are characterized by frequent turns and loops at higher memory, when walker localization is observed, but become more rectilinear at low memory, when the walker motion is more diffusive (Supplemental Material Video 2 [17]). For illustrative purposes, here we increase the memory up to 99.8%, which is the experimental value but higher than what is numerically feasible for the long-time statistics shown in Figs. 2(h) and 2(i). (b) Visualization of the wave field in our experiments reveals the emergence of beams connecting the droplet and localization region (yellow dashed line) that draw the droplet in. Once inside the localization region, the superposition of slowly decaying waves traps the droplet in loops that significantly increase the trapping time. (c) Similar wave-mediated interactions are observed in our walker simulations. (d) The attracting beams and trapping waves are more apparent in the topography-induced wave perturbation, $\xi = \eta - \bar{\eta}$, obtained by subtracting from the wave field η, shown in (c), the computed wave field $\bar{\eta}$ of a droplet following the same trajectory in a homogeneous bath of the same base depth, H_0. The wave fields in (b) and (c) are strobed at the Faraday frequency with a phase at which the waves are near their maximum amplitude. See Supplemental Material Video 3 [17] for video animations of (b)–(d).

examine the walker dynamics at low memory, $\gamma/\gamma_F = 77\%$, when the wave field is less extensive, $l \sim 2\lambda_F$, and decays quickly, $T_M \sim 0.23$ s. The particle's average speed is maintained by readjusting the impact phase (Appendix D). In this regime, droplets move freely throughout the heterogeneous media [Figs. 2(e) and 2(f)], indicating a diminished influence of the submerged topography on the wave field. As the memory decreases, the walker dynamics thus approaches the diffusive behavior of the waveless particle. We perform analogous simulations over a range of memories and quantify the walker's diffusive behavior through the MSD's asymptotic dependence on time [2], $\langle r^2(t)\rangle \sim t^\alpha$ [Fig. 2(h)]. As the memory is increased, we observe a progressive suppression of diffusion, from a conducting state ($\alpha \to 1$) at low memory to a localized state ($\alpha \to 0$) when the forcing acceleration is near the Faraday threshold [Fig. 2(i)].

IV. WAVE-MEDIATED MECHANISM

To rationalize the walker dynamics that result in localized statistics, which exhibits frequent turns with a preferred radius of curvature as the memory increases [Fig. 3(a)], we investigate the droplet-topography interaction mechanism through examination of the wave field. At any instant, the wave field is complex, the result of a superposition of waves created by the droplet's previous bounces [34]. Yet, both experiments [Fig. 3(b)] and simulations [Fig. 3(c)] show two distinct wave-mediated resonant effects responsible for localization. These effects become more evident in the topography-induced, or "anomalous" [35], wave field, $\xi(\boldsymbol{x}, t) = \eta - \bar{\eta}$ [Fig. 3(d)], obtained by subtracting from the simulated wave field η [Fig. 3(c)] that of the droplet following the same path in a homogeneous layer of the same base depth, $\bar{\eta}$. First, when the localization region is within range of the walker wave field, beamlike waves [35] connecting the droplet and the localization region draw the droplet in. Second, once the droplet reaches the localization region, relatively larger waves are excited, which force the droplet to execute multiple loops, thus increasing the trapping time [Fig. 3(d)]. These wave-mediated effects, thus, produce spatiotemporally nonlocal forces [41] on the droplet that result in a peak in the position histogram. At low memory, when the walker motion is more diffusive, the relative extent and magnitude of the attracting beams and trapping waves are significantly diminished (Fig. 11).

To understand the resonant waves that emanate from the localization region, which acts as an area of high excitability, we visualize experimentally the hydrostatic free surface at the instability threshold, $\gamma = \gamma_F$, in the absence of the droplet [Fig. 4(a) and Supplemental Material Video 3 [17]]. The localization region corresponds to the location where the first Faraday waves are observed, which bear a resemblance to the beamlike waves that are occasionally excited in the anomalous walker wave field [Fig. 3(d)].

We also observe a correspondence between the droplet histogram and the mean pilot wave [34], $\langle\eta\rangle$, which is characterized by the superposition of Faraday waves about a relatively wide depression centered at the localization region [Fig. 4(b)] [43]. The spectrum of the mean wave field [Fig. 4(c)] highlights a separation of length scales, consisting of near-critical standing Faraday waves and long traveling waves emanating from each droplet impact [33]. Under the assumptions of ergodicity and wave linearity, we may rationalize the form of the mean wave field in terms of the droplet histogram, $p_s(\boldsymbol{x})$, via the relationship [43,44]

$$\langle\eta\rangle(\boldsymbol{x}) = \iint_{\mathcal{D}} p_s(\boldsymbol{x}')\eta_B(\boldsymbol{x}, \boldsymbol{x}')\mathrm{d}\boldsymbol{x}', \tag{2}$$

where $\eta_B(\boldsymbol{x}, \boldsymbol{x}_p)$ is the wave field generated by a bouncer at position $\boldsymbol{x}_p$ in the domain $\mathcal{D}$. By decomposing η_B into its long and Faraday wave components, which may be approximated through the analysis of the quasipotential waves model (1) (Appendix B), we use Eq. (2) to numerically reconstruct the mean wave field separately and so discern the features produced by each type of mode. While unimportant for pilot-wave dynamics in a homogeneous bath, the reconstructed mean wave field using the long-wave modes indicates that the complex reflection and transmission of long traveling waves over disordered media

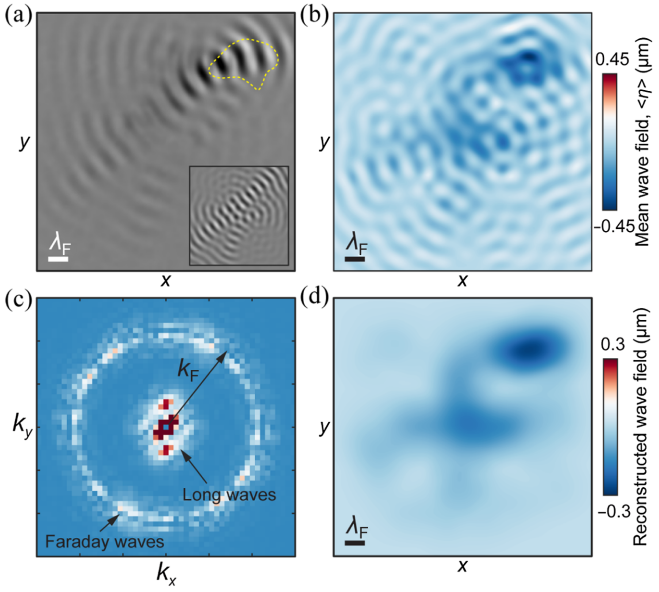

FIG. 4. Superposition of long-wave modes rationalizes the mean wave field. (a) Experimental Faraday waves observed at threshold, $\gamma = \gamma_F$, emanating from the localization area (yellow dashed line), which agrees with the theoretical Faraday mode (inset). (b) The mean (time-averaged) pilot wave $\langle\eta\rangle$, computed from simulations matching the experiment [Fig. 9(c)], shows a large depression at the localization region. (c) The spectrum of the mean wave is composed of subcritical Faraday modes and long waves, which may be obtained theoretically from the walker wave model (1). (d) The same large-scale envelope, which acts as an effective potential, is reconstructed from the position histogram and long-wave modes according to Eq. (2).

play a significant role in the walker localization, producing an effective long-range potential about the localization region that contributes to the sustained trapping of the droplet [Fig. 4(d)] [43]. Notably, this bowl-shaped potential cannot be generated solely by the Faraday modes, whose elevation instead approximately vanishes when averaged over each wavelength. Furthermore, a perturbative Floquet analysis of the system's Faraday modes demonstrates that the mean Faraday waves are of a highly complex form and do not closely resemble any of the near-critical Faraday modes (Appendix B 4 d). The mean wave field may, thus, be regarded as a long-wave potential modulated by a unstructured high-frequency scatter of Faraday waves across the disordered medium.

V. CONCLUSIONS

While Anderson localization has been realized in numerous systems of classical waves [18–28], the original electronic localization is distinct, because it incorporates the notion of a particle effectively coming to a halt due to the landscape disorder [11–15]. We have demonstrated that, owing to the resonant interaction with its self-excited wave field, walking droplets over random topographies may exhibit *dual* wave-particle localization analogous to that of subatomic particles in disordered media. The walker localization is observed in the high-memory regime, as the extent of the walker's wave field becomes comparable to that of the Faraday mode of the topography, and the waves persist for a relatively long period of time. The waves excited by the droplet at each impact form an effective wave potential that draws the droplet toward the localization region, where it resonates with the most unstable cavity mode, causing the droplet to execute loops at relatively high speed. At low memory, when the walker's wave field is small and decays relatively quickly, the droplet can easily traverse the random topography, ultimately exhibiting diffusive motion. In a broader context, the suppression of diffusion observed in the walker system as the memory increases invites the investigation of localization effects in other active systems with memory effects [45,46] and wave-guided motion, including those realized with stratified flows [47], canoes [48], capillary surfers [49], and acoustically forced bubbles [50]. The dual wave-particle localization of walking droplets also motivates new directions of research in wave [29,51] and many-body [52,53] localization, as well as topological active matter [5,54,55].

The data that support the findings of this study are available from the corresponding author upon reasonable request.

ACKNOWLEDGMENTS

The authors thank Rodolfo R. Rosales for enlightening discussions. P. J. S. gratefully acknowledges financial support from the Alfred P. Sloan Foundation (Sloan Research Fellowship) and U.S. National Science Foundation (CAREER Award No. CBET-2144180). A. J. A. gratefully acknowledges financial support from UNC's Office of Undergraduate Research (Summer Undergraduate Research Fellowship).

APPENDIX A: EXPERIMENTS

We describe here the experimental setup (Appendix A 1) and data acquisition protocol (Appendix A 2) adopted to obtain the results presented in the main text.

1. Experimental setup

A schematic of the experimental setup is presented in Fig. 5. The random topography is composed of a regular grid of 13×13 square tiles, each with a width $W = 5.25$ mm (matching the Faraday wavelength, λ_F) and a random height drawn from the uniform distribution in the interval $\Delta H = \pm 0.3$ mm. The topography includes 4×4 regularly spaced pillars with height $\Delta H = 0.6$ mm to facilitate data acquisition; the pillars play no significant role in the localization problem (Appendix D 1 d). The variable topography is 3D printed with a FormLabs Form 3+ stereolithography printer (25 μm XY resolution, 25 μm minimum layer thickness, 85 μm laser spot size, black photopolymer resin FormLabs V4) with a minimum base thickness of 0.25 mm and vertically oriented to minimize height deformations during the curing process. The prints are washed for 30 min in isopropanol beforehand and later cured for 30 min under UV light at 60 °C. The print supports are kept on the parts during the curing process to provide extra stability, thus minimizing warping due to thermal expansion.

The random topography is bolted to the base of a circular aluminum bath, which is later filled with silicone oil with density $\rho = 950$ kg m^{-3}, viscosity $\nu = 20.9$ cSt, and surface tension $\sigma = 20.6$ mN m^{-1}. The heterogeneous domain, with base depth $H_0 = 1.85$ mm, is surrounded by a shallower liquid layer, with uniform depth $H_1 = 1.20$ mm and minimum width $D_1 = 30.5$ mm, which prevents the droplet from escaping the region of interest. An additional outer layer of depth $H_2 = 1.10$ mm and width $D_2 = 35.6$ mm is located between the 3D printed topography and the bath's wall to damp the meniscus waves [56]. The aluminum bath is sealed with a transparent acrylic lid to ensure that external air currents do not influence the experiment.

The bath is subject to vertical sinusoidal oscillations with frequency $f = \omega_0/2\pi = 70$ Hz using a state-of-the-art vibrating setup [57] whose precision has enabled the characterization of the walker dynamics in numerous settings [30,58]. Specifically, the aluminum bath is mounted to a linear air bearing (PI L.P., $4 \times 4''$ cross section, $6.5''$ long hollow bar) connected to an air-cooled electromagnetic shaker (Modal Shop, 2110E) powered by

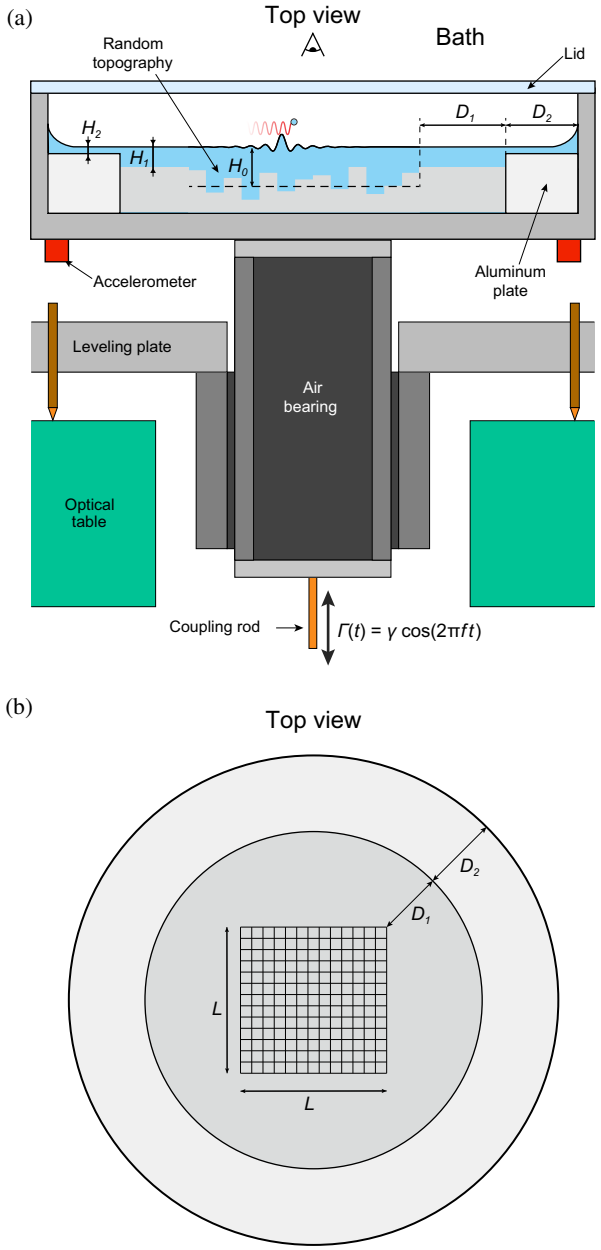

FIG. 5. Schematic of the experimental setup. (a) The test section is mounted on an optical table and vibrated vertically by an electromagnetic shaker. The shaker is connected to the bath by a thin steel rod coupled with a linear air bearing to minimize lateral vibrations. The forcing acceleration is monitored by two piezoelectric accelerometers. The bath is sealed with a transparent acrylic lid to ensure that ambient air currents do not affect the experiments. (b) The square random topography of width $L = 68.25$ mm is surrounded by a shallow layer of depth $H_1 = 1.20$ mm and minimum width $D_1 = 30.5$ mm and a thinner damping layer of depth $H_2 = 1.10$ mm and width $D_2 = 35.6$ mm to prevent meniscus waves from influencing the droplet dynamics.

an external power amplifier (Modal Shop, 2050E09-FS). The air bearing rests on an optical table (Newport, custom SG-34-4 breadboard, $3.0' \times 4.0' \times 4.32''$, centered $8.00''$ diameter access hole) for high-precision leveling through three micrometer screws (Newport, AJS100-1H). The shaker is connected to the inner slide bar of the air bearing through a thin coupling rod (diameter 1.6 mm and length 60 mm) with very low lateral stiffness to prevent any nonaxial vibration generated by the shaker from being transmitted to the payload. Two piezoelectric accelerometers (PCB, 352C65) mounted in diametrically opposed locations atop the slider bar measure the vibration amplitude, which is specified and monitored through a custom closed-feedback loop developed using a data acquisition system (NI, USB-6343) and LABVIEW software. This setup [57] avoids undesirable resonances and multidirectional vibrations, achieving a precision of the driving acceleration of $\pm 0.002g$ and spatially uniform vibration within 0.1%.

We use a piezoelectric droplet-on-demand generator [59] to produce droplets of the same silicone oil and reproducible size (radius $R = 0.371 \pm 0.003$ mm). The bath is illuminated with a LED light ring to increase the contrast between the drops and the black background. The motion of the walking droplet is recorded at 10 frames per second with a CCD camera (AV Mako U-130B USB3, Mono, 6.2 px/mm) mounted directly above the bath and tracked with an in-house particle-tracking algorithm written in MATLAB. The form of the wave field is captured by recording the normal reflection of light at the free surface [56] through a semireflective mirror placed at 45° between the CCD camera and the bath. For the wave visualization, the light ring is replaced by a square diffuse-light lamp facing the mirror horizontally. One then observes images with bright regions corresponding to horizontal parts of the surface, extrema, or saddle points [56].

2. Data acquisition

We define the Faraday threshold $\gamma_F = 3.775g$ as the critical vibrational acceleration at which Faraday waves [60] are first observed above the localization region in the absence of the droplet. To ensure a steady state in the bath, the experimental setup is left vibrating at $\gamma \approx \gamma_F$ for at least 2 h before conducting any experiment. The droplet motion is recorded for 6 h in 20-min intervals. The length of the interval is selected to maintain the prescribed memory, $\gamma/\gamma_F = 99.8 \pm 0.1\%$, which may drift slowly due to weak variations in viscosity and surface tension resulting from ambient temperature changes. The Faraday threshold is measured before and after each experimental run to ensure that the Faraday threshold is never crossed. Thus, no waves exist in the bath in the absence of the droplet. We record the droplet motion for 6 h in total, which corresponds to approximately 750 000 bounces and roughly 2300 domain crossings for the average speed $v_0 = 7.3$ mm/s.

At the prescribed forcing acceleration, the memory time [33] is $T_M = T_d/(1 - \gamma/\gamma_F) \approx 26$ s, where $T_d = \lambda_F^2/(8\pi^2\nu) \approx 0.0525$ s is the characteristic wave decay time in the absence of vibrational forcing [32]. The memory time is, thus, negligible relative to length of the recording

intervals, which guarantees that the emergent statistics are not influenced by initial conditions. We also confirm ergodicity with our accompanying walker simulations (Appendix D).

Faraday waves are subharmonic, oscillating at half of the prescribed vibrational frequency. The Faraday wavelength $\lambda_F = 2\pi/k_F$ may, thus, be obtained through the capillary-gravity dispersion relation [37] $\omega_0^2/4 = (gk_F + \sigma k_F^3/\rho)\tanh(k_F H)$, where g is the gravitational acceleration and H is the fluid depth. For the base depth $H_0 = 1.85$ mm, the characteristic Faraday wavelength is $\lambda_F = 5.23$ mm. The difference in λ_F due to the maximum depth variations ($\Delta H = \pm 0.3$ mm) and pillars ($\Delta H = +0.6$ mm) is at most 1% and 3%, respectively.

We estimate the walker's spatial extent l, or "damping length" [38], through direct visualization of the experimental wave field at the prescribed memory. Our measurements, $l \approx 7\lambda_F$, are in the same order as the damping length predicted by theory [38].

APPENDIX B: THEORY

We combine simulations and analytical techniques to characterize the dynamics and statistics of the walking droplet system. We first describe a reduced theoretical model (Appendix B 1), which forms the basis of our simulations and accompanying analysis. To distinguish the prevailing features of this pilot-wave system, we decompose the fluid evolution into the dynamics of long waves and Faraday modes (Appendix B 2), the latter of which is approximated using Floquet theory (Appendix B 3). Finally, we characterize the manifestation of long waves and Faraday modes in the formation of the time-averaged pilot-wave arising when the system is in statistical equilibrium (Appendix B 4).

1. Pilot-wave model

We present a reduced theoretical model [42] of the pilot-wave system evolving over variable topography, which we utilize to buttress experimental observations and shed light on the dynamical and statistical features of the pilot-wave system.

a. Fluid evolution

The fluid evolution is governed by the quasipotential flow model [61,62] for the free-surface elevation $\eta(\boldsymbol{x}, t)$ and the linearized free-surface velocity potential $u(\boldsymbol{x}, t) = \phi(\boldsymbol{x}, 0, t)$, where $\phi(\boldsymbol{x}, z, t)$ satisfies Laplace's equation in the fluid bulk, with no-flux boundary conditions on the submerged topography. In the vibrating frame of reference, u and η evolve according to

$$u_t = -G(t)\eta + \frac{\sigma}{\rho}\Delta\eta + 2\nu\Delta u - \frac{P}{\rho}, \tag{B1a}$$

$$\eta_t = \mathcal{L}u + 2\nu\Delta\eta, \tag{B1b}$$

where σ is the coefficient of surface tension, ρ is the fluid density, ν is the fluid kinematic viscosity, P is the pressure exerted by the droplet on the free surface (defined in Appendix B 1 b), and $\mathcal{L}$ is the Dirichlet-to-Neumann operator, defined $\mathcal{L}\phi|_{z=0} = \phi_z|_{z=0}$. As a consequence of expressing the fluid evolution in the vibrating frame of reference, we define $G(t) = g - \gamma\cos(\omega_0 t)$ as the effective gravitational acceleration, where ω_0 is the angular frequency, g is the gravitational acceleration in the absence of vibrational forcing, and γ is the peak vibrational acceleration.

We adopt the formulation of Faria [42], who, informed by shallow-water theory, approximated the Dirichlet-to-Neumann operator for variable topography by the phenomenological operator $\mathcal{L} = -\nabla\cdot b(\boldsymbol{x})\nabla$, where the effective depth $b(\boldsymbol{x})$ is defined in terms of the actual fluid depth $H(\boldsymbol{x})$. Specifically,

$$b(\boldsymbol{x}) = \frac{\tanh[k_c(\boldsymbol{x})H(\boldsymbol{x})]}{k_c(\boldsymbol{x})}$$

and $k_c = \mathrm{argmin}_k \gamma_c(k)$ is the critical wave number for each value of $\boldsymbol{x}$, where [61]

$$\gamma_c^2(k) = \frac{4g^2}{\omega_g^4(k)}\left(\left[\omega^2(k) + \mu^2(k) - \frac{\omega_0^2}{4}\right]^2 + \omega_0^2\mu(k)^2\right)$$

determines the neutral stability curve, $\omega^2(k) = k\tanh(kH)(g + \sigma k^2/\rho)$ is the finite-depth gravity-capillary dispersion relation, $\mu(k) = 2\nu k^2$ determines wave damping, and $\omega_g^2(k) = gk\tanh(kH)$ is the finite-depth dispersion relation for gravity waves.

b. Wave-droplet coupling

We model the wave-droplet coupling by prescribing instantaneous periodic impacts [42,63] at times $t_n = nT_F + \theta_I/\omega_0$ (for $n = 0, 1, 2, \ldots$), where $T_F = 4\pi/\omega_0$ is the Faraday period and θ_I is the impact phase. We, thus, prescribe an interaction force of the form

$$F(t) = mgT_F\sum_{n=0}^{\infty}\delta(t - t_n), \tag{B2}$$

where $m = \frac{4}{3}\pi\rho R^3$ is the droplet mass, R is the droplet radius, and δ is the Dirac delta function [42,63]. Moreover, we prescribe that the pressure P exerted on the free surface during each impact is localized to a point in space about the droplet's current position, $\boldsymbol{x}_p(t)$, namely, $P(\boldsymbol{x}, t) = F(t)\delta[\boldsymbol{x} - \boldsymbol{x}_p(t)]$ [42,63]. We model the droplet's horizontal motion according to [32]

$$m\ddot{\boldsymbol{x}}_p + D(t)\dot{\boldsymbol{x}}_p = -F(t)\nabla\eta(\boldsymbol{x}_p, t), \tag{B3}$$

where

$$D(t) = c_4\sqrt{\frac{\rho R}{\sigma}}F(t) + 6\pi R\mu_{\text{air}}$$

is the drag acting on the droplet, μ_{air} is the dynamic viscosity of air, and c_4 is the coefficient of tangential restitution. During droplet flight, i.e., $t_n < t < t_{n+1}$, the coupling force vanishes, i.e., $F(t) = 0$, and the droplet inertia is balanced by Stokes drag. Across each impact, we apply the jump condition in the droplet's velocity:

$$[\dot{\boldsymbol{x}}_{\text{p}}(t_n)]^{+}_{-} = -(1-\text{e}^{-C})\left(\frac{gT_F}{C}\nabla\eta[\boldsymbol{x}_{\text{p}}(t_n), t_n] + \dot{\boldsymbol{x}}_{\text{p}}(t_n^{-})\right), \tag{B4}$$

where $C = c_4 g T_{\text{F}}\sqrt{\rho R/\sigma}$ [42,63].

2. Wave field evolution

We start by transforming Eq. (B1) into Fourier space, for which we find that the conjugate variables $\hat{u}(\boldsymbol{k}, t)$ and $\hat{\eta}(\boldsymbol{k}, t)$ evolve according to

$$\hat{u}_t = -G(t)\hat{\eta} - \frac{\sigma}{\rho}|\boldsymbol{k}|^2\hat{\eta} - 2\nu|\boldsymbol{k}|^2\hat{u} - \frac{F(t)}{\rho}\text{e}^{-\text{i}\boldsymbol{k}\cdot\boldsymbol{x}_{\text{p}}}, \tag{B5a}$$

$$\hat{\eta}_t = \hat{\mathcal{L}}_{\boldsymbol{k}}\,\hat{u} - 2\nu|\boldsymbol{k}|^2\hat{\eta}, \tag{B5b}$$

where $\boldsymbol{k}$ is the wave vector and $\hat{\mathcal{L}}_{\boldsymbol{k}}$ is the Fourier symbol of the operator $\mathcal{L}$. For Faria's model, $\hat{\mathcal{L}}_{\boldsymbol{k}}\,\hat{u} = \boldsymbol{k}\cdot\mathcal{F}[b(\boldsymbol{x})\mathcal{F}^{-1}[\boldsymbol{k}\hat{u}]]$, where $\mathcal{F}$ and $\mathcal{F}^{-1}$ represent the forward and inverse Fourier transforms, respectively [42]. We consider the fluid evolution on a doubly periodic domain using the discrete Fourier transform, giving rise to the nonzero discrete wave vectors $\boldsymbol{k}_j$ for $j = 1, \ldots, \mathcal{N}$. We exclude the zero wave vector from this set as conservation of mass implies that $\hat{\eta}(\boldsymbol{0}, t) = 0$ and additive invariance of the velocity potential means that we may choose $\hat{u}(\boldsymbol{0}, t) = 0$. We proceed now to reformulate the system (B5) as a matrix-vector system in Floquet form.

By defining row vectors $\hat{\boldsymbol{u}}(t)$ and $\hat{\boldsymbol{\eta}}(t)$ with elements $\hat{u}(\boldsymbol{k}_j, t)$ and $\hat{\eta}(\boldsymbol{k}_j, t)$, respectively, we may thus express Eq. (B5) in matrix-vector form:

$$\frac{\text{d}\boldsymbol{v}}{\text{d}t} = \Big(\boldsymbol{A} + \gamma\cos(\omega_0 t)\boldsymbol{B}\Big)\boldsymbol{v} - \boldsymbol{F}(t), \tag{B6a}$$

where $\boldsymbol{v} = (\hat{\boldsymbol{u}}, \hat{\boldsymbol{\eta}})^T$,

$$\boldsymbol{A} = \begin{pmatrix} -2\nu\boldsymbol{K}^2 & -(g\boldsymbol{I} + \sigma\rho^{-1}\boldsymbol{K}^2) \\ \boldsymbol{L} & -2\nu\boldsymbol{K}^2 \end{pmatrix}, \tag{B6b}$$

$\boldsymbol{K}$ is a diagonal matrix with elements $|\boldsymbol{k}_j|$, $\boldsymbol{I}$ is the identity matrix, $\boldsymbol{L}$ is a matrix representing the Fourier symbol of the operator $\mathcal{L}$, and

$$\boldsymbol{B} = \begin{pmatrix} \boldsymbol{0} & \boldsymbol{I} \\ \boldsymbol{0} & \boldsymbol{0} \end{pmatrix}. \tag{B6c}$$

Finally, the forcing term $\boldsymbol{F}(t)$ in Eq. (B6a) represents the Fourier transform of the pressure, namely,

$$\boldsymbol{F}(t) = \frac{F(t)}{\rho}\begin{pmatrix} \boldsymbol{e}[\boldsymbol{x}_{\text{p}}(t)] \\ \boldsymbol{0} \end{pmatrix},$$

where $\boldsymbol{e}(\boldsymbol{x})$ is a column vector (of length $\mathcal{N}$) with elements $\text{e}^{-\text{i}\boldsymbol{k}_j\cdot\boldsymbol{x}}$. Between successive impacts, the coupling force vanishes, i.e., $\boldsymbol{F}(t) = \boldsymbol{0}$. By assuming that $\boldsymbol{x}_{\text{p}}(t)$ is continuous across each impact, we use Eq. (B6a) to derive the jump condition $[\boldsymbol{v}(t_n)]^{+}_{-} = -\boldsymbol{f}_n$ [42,63], where $\boldsymbol{f}_n = \boldsymbol{f}[\boldsymbol{x}_{\text{p}}(t_n)]$ and

$$\boldsymbol{f}(\boldsymbol{x}) = \frac{mgT_{\text{F}}}{\rho}\begin{pmatrix} \boldsymbol{e}(\boldsymbol{x}) \\ \boldsymbol{0} \end{pmatrix}. \tag{B7}$$

Our investigation is focused, henceforth, on the computational analysis of Eq. (B6), which governs the evolution of the $2\mathcal{N}$ complex variables describing the fluid state.

a. Wave field decomposition

In the absence of vibrational forcing, the quasipotential flow model (B1) exhibits a viscous damping rate of $2\nu|\boldsymbol{k}|^2$ for each Fourier mode, corresponding to the relatively slow decay of long traveling waves. When the vibrational acceleration is instead just below that of the Faraday threshold, the slow decay of long waves ($|\boldsymbol{k}| \ll k_{\text{F}}$) persists, and the decay time of the Faraday modes ($|\boldsymbol{k}| \approx k_{\text{F}}$) increases, dilating with increased proximity to the Faraday threshold (see Appendix B 3). The wave field generated by a walking droplet is, thus, composed of both long traveling waves and shorter standing waves (Faraday modes) [61]. We proceed to exploit the separation of length scale exhibited by the long waves and Faraday modes to decompose the fluid evolution into a long-wave model and an approximation for near-critical Faraday modes. Specifically, we consider $\boldsymbol{v} \approx \boldsymbol{v}_{\text{L}} + \boldsymbol{v}_{\text{F}}$, where we determine an approximate evolution equation for the long waves, denoted $\boldsymbol{v}_{\text{L}}$, in Appendix B 2 b and determine an approximate solution for the near-critical Faraday modes, denoted $\boldsymbol{v}_{\text{F}}$, in Appendix B 3. We then combine our analytical results to characterize the manifestation of long waves and Faraday waves in both the instantaneous and time-averaged pilot wave.

b. Evolution of long waves

The submerged topography is shallow relative to the long-wave modes, and so the critical vibrational forcing for

long waves ($|\boldsymbol{k}| \ll k_{\mathrm{F}}$) vastly exceeds that of the Faraday threshold. Specifically, the magnitude of their critical vibrational threshold has size $O(k^{-2})$ as $k \to 0$ [64]. Hence, when the vibrational forcing is just below the Faraday threshold, the parametric forcing has only a weak effect on the evolution of long waves. A leading-order approximation for long waves is, thus, afforded by setting $\gamma = 0$ in the quasipotential flow equations (B1), indicating that $\boldsymbol{v}_{\mathrm{L}}$ evolves according to

$$\frac{\mathrm{d}\boldsymbol{v}_{\mathrm{L}}}{\mathrm{d}t} = \boldsymbol{A}\boldsymbol{v}_{\mathrm{L}} - \boldsymbol{F}(t), \tag{B8}$$

where the forcing $\boldsymbol{F}(t)$ vanishes during flight ($t_n < t < t_{n+1}$) and gives rise to the jump condition $[\boldsymbol{v}_{\mathrm{L}}(t_n)]^{+}_{-} = -\boldsymbol{f}_n$ across each impact. We note that waves that are not long are strongly damped when $\gamma = 0$, owing to the dissipation rate $2\nu|\boldsymbol{k}|^2$, and so have a negligible role in the resulting dynamics.

3. Evolution of Faraday modes

We proceed to seek approximate solutions for near-critical Faraday modes satisfying

$$\frac{\mathrm{d}\boldsymbol{v}_{\mathrm{F}}}{\mathrm{d}t} = \left(\boldsymbol{A} + \gamma\cos(\omega_0 t)\boldsymbol{B}\right)\boldsymbol{v}_{\mathrm{F}} - \boldsymbol{F}(t), \tag{B9}$$

where the forcing $\boldsymbol{F}(t)$ vanishes during flight ($t_n < t < t_{n+1}$) and gives rise to the jump condition $[\boldsymbol{v}_{\mathrm{F}}(t_n)]^{+}_{-} = -\boldsymbol{f}_n$ across each impact. Owing to the periodic parametric forcing, $\gamma\cos(\omega_0 t)\boldsymbol{B}$, we observe that Eq. (B9) is of Floquet form during droplet flight. We, thus, use Floquet theory to approximate the evolution of the near-critical Faraday modes during droplet flight, giving rise to a reduced framework for characterizing the manifestation of Faraday modes in the instantaneous and time-averaged pilot wave. We formulate the Floquet analysis in Appendix B 3 a, before determining the critical vibration of each Faraday mode (Appendix B 3 b) and the corresponding near-critical decay rate (Appendix B 3 c).

a. Approximating Faraday modes

For any fixed value of $\gamma \neq 0$, we deduce from Floquet theory that $\boldsymbol{v}_{\mathrm{F}}(t)$ has linearly independent solutions

$$\boldsymbol{v}_{\mathrm{F},j}(t) = \boldsymbol{p}_j(t)\mathrm{e}^{\lambda_j t} \quad \text{for } j = 1, \ldots, 2\mathcal{N}, \tag{B10}$$

where $\boldsymbol{p}_j(t)$ is a periodic function of period T_{F} and $\lambda_j(\gamma)$ is a Floquet exponent. We may represent $\boldsymbol{p}_j(t)$ as a Fourier series and use as many terms as necessary in the truncated series expansion for the predicted Faraday threshold (and associated mode) to converge [37,64]. However, we find that a favorable, and computationally tractable, approximation of the Faraday modes is afforded by considering only the leading-order frequencies in the Fourier series of $\boldsymbol{p}_j(t)$, an assumption that has been utilized throughout the walking-droplet literature [32,61].

We proceed by writing

$$\boldsymbol{p}_j(t) = \boldsymbol{x}_j \sin\left(\frac{\omega_0 t}{2}\right) + \boldsymbol{y}_j \cos\left(\frac{\omega_0 t}{2}\right), \tag{B11}$$

where $\boldsymbol{x}_j(\gamma)$ and $\boldsymbol{y}_j(\gamma)$ are as-yet-undetermined nonzero vectors, and then we substitute Eqs. (B10) and (B11) into Eq. (B9) and simplify the resultant expressions. By using the identities

$$2\cos(2\theta)\cos\theta = \cos(3\theta) + \cos\theta,$$
$$2\cos(2\theta)\sin\theta = \sin(3\theta) - \sin\theta,$$

we obtain the system of equations

$$\begin{aligned}&\left[-\frac{\omega_0}{2}\boldsymbol{y}_j + \lambda_j\boldsymbol{x}_j - \boldsymbol{A}\boldsymbol{x}_j + \frac{\gamma}{2}\boldsymbol{B}\boldsymbol{x}_j\right]\sin\left(\frac{\omega_0 t}{2}\right)\mathrm{e}^{\lambda_j t}\\ &\quad + \left[\frac{\omega_0}{2}\boldsymbol{x}_j + \lambda_j\boldsymbol{y}_j - \boldsymbol{A}\boldsymbol{y}_j - \frac{\gamma}{2}\boldsymbol{B}\boldsymbol{y}_j\right]\cos\left(\frac{\omega_0 t}{2}\right)\mathrm{e}^{\lambda_j t}\\ &\quad + \text{higher harmonics} = 0.\end{aligned}$$

By neglecting the higher harmonics, consistent with our leading-order frequency approximation, and utilizing the linear independence of the functions $\sin(\frac{1}{2}\omega_0 t)\mathrm{e}^{\lambda_j t}$ and $\cos(\frac{1}{2}\omega_0 t)\mathrm{e}^{\lambda_j t}$, we find that $\boldsymbol{x}_j$ and $\boldsymbol{y}_j$ satisfy

$$-\frac{\omega_0}{2}\boldsymbol{y}_j + \lambda_j\boldsymbol{x}_j - \boldsymbol{A}\boldsymbol{x}_j + \frac{\gamma}{2}\boldsymbol{B}\boldsymbol{x}_j = \boldsymbol{0}, \tag{B12a}$$

$$\frac{\omega_0}{2}\boldsymbol{x}_j + \lambda_j\boldsymbol{y}_j - \boldsymbol{A}\boldsymbol{y}_j - \frac{\gamma}{2}\boldsymbol{B}\boldsymbol{y}_j = \boldsymbol{0}. \tag{B12b}$$

To further simplify, we eliminate $\boldsymbol{y}_j$ by premultiplying Eq. (B12a) by $[\lambda_j\boldsymbol{I} - \boldsymbol{A} - (\gamma/2)\boldsymbol{B}]$ and utilizing Eq. (B12b); we, thus, arrive at the condition $\boldsymbol{M}(\lambda_j, \gamma)\boldsymbol{x}_j = \boldsymbol{0}$, where

$$\boldsymbol{M}(\lambda, \gamma) = \frac{\omega_0^2}{4}\boldsymbol{I} + \left[\boldsymbol{A} - \lambda\boldsymbol{I} + \frac{\gamma}{2}\boldsymbol{B}\right]\left[\boldsymbol{A} - \lambda\boldsymbol{I} - \frac{\gamma}{2}\boldsymbol{B}\right]. \tag{B13}$$

The vector $\boldsymbol{y}_j$ may then be recovered from Eq. (B12), from which one may then determine the sinusoidal oscillation of the fluid, $\boldsymbol{p}_j(t)$.

For given $\gamma \neq 0$, we seek a series of nonzero vectors $\boldsymbol{x}_j(\gamma)$ and growth rates $\lambda_j(\gamma)$ defined by the nonlinear eigenvalue problem $\boldsymbol{M}(\lambda_j, \gamma)\boldsymbol{x}_j = \boldsymbol{0}$. Then, we define the critical vibrational forcing γ_j for each mode, with $\lambda_j(\gamma_j) = 0$, and denote $\boldsymbol{x}_{j,0} = \boldsymbol{x}_j(\gamma_j)$. We now develop methodologies for (i) determining γ_j and $\boldsymbol{x}_{j,0}$ (Appendix B 3 b) and (ii) determining $\lambda_j(\gamma)$ and $\boldsymbol{x}_j(\gamma)$ for $|\gamma - \gamma_j|/g \ll 1$ (Appendix B 3 c). These results are then applied to the computation of the mean pilot wave in Appendix B 4.

b. Critical forcing for each mode

The critical vibrational forcing γ_j for each eigenmode, denoted $\boldsymbol{x}_{j,0} \neq \boldsymbol{0}$, arises when the corresponding decay rate vanishes, i.e., $\lambda_j = 0$, with $\boldsymbol{M}(0,\gamma_j)\boldsymbol{x}_{j,0} = \boldsymbol{0}$. In order to determine γ_j and $\boldsymbol{x}_{j,0}$, we rearrange Eq. (B13) and note that $\boldsymbol{B}^2 = \boldsymbol{0}$, giving

$$\boldsymbol{M}(0,\gamma) = \frac{\omega_0^2}{4}\boldsymbol{I} + \boldsymbol{A}^2 + \frac{\gamma}{2}[\boldsymbol{BA} - \boldsymbol{AB}].$$

From $\boldsymbol{M}(0,\gamma_j)\boldsymbol{x}_{j,0} = \boldsymbol{0}$, we deduce that

$$\left(\boldsymbol{A}^2 + \frac{\omega_0^2}{4}\boldsymbol{I}\right)\boldsymbol{x}_{j,0} = \frac{\gamma_j}{2}[\boldsymbol{AB} - \boldsymbol{BA}]\boldsymbol{x}_{j,0}.$$

Finally, by writing

$$\mathcal{A} = \boldsymbol{A}^2 + \frac{\omega_0^2}{4}\boldsymbol{I} \quad \text{and} \quad \mathcal{B} = \frac{1}{2}[\boldsymbol{AB} - \boldsymbol{BA}],$$

we observe that $\boldsymbol{M}(0,\gamma_j)\boldsymbol{x}_{j,0} = \boldsymbol{0}$ reduces to the generalized eigenvalue problem $\mathcal{A}\boldsymbol{x}_{j,0} = \gamma_j\mathcal{B}\boldsymbol{x}_{j,0}$, where γ_j is an eigenvalue (indexed by j) and $\boldsymbol{x}_{j,0}$ is a corresponding eigenvector. It is expedient, however, to reformulate the generalized eigenvalue problem as [37,64]

$$\mathcal{A}^{-1}\mathcal{B}\boldsymbol{x}_{j,0} = \frac{1}{\gamma_j}\boldsymbol{x}_{j,0}, \tag{B14}$$

from which it follows that γ_j is the reciprocal of an eigenvalue of the matrix $\mathcal{A}^{-1}\mathcal{B}$.

Notably, choosing to instead eliminate $\boldsymbol{x}_j$ from system (B12) gives rise to the similar relationship

$$\mathcal{A}^{-1}\mathcal{B}\boldsymbol{y}_{j,0} = -\frac{1}{\gamma_j}\boldsymbol{y}_{j,0}.$$

We, thus, deduce that if α is an eigenvalue of the matrix $\mathcal{A}^{-1}\mathcal{B}$, then so is $-\alpha$. Consequently, the critical thresholds appear in negated pairs, consistent with the invariance of the fluid system (B1) under the mapping $(t,\gamma) \mapsto (t + \pi/\omega_0, -\gamma)$. Modes with $\gamma_j > 0$ are damped for $\gamma < \gamma_j$ and excited for $\gamma > \gamma_j$; in contrast, modes with $\gamma_j < 0$ are excited for $\gamma < \gamma_j$ and damped for $\gamma > \gamma_j$. When considering $\gamma > 0$, we conclude that modes satisfying $\gamma_j < 0$ are strongly damped.

c. Mode decay rates

For the remainder of this section, we restrict our attention to the case $\gamma > 0$ and define the Faraday threshold $\gamma_{\mathrm{F}} = \min_j |\gamma_j|$. For a given value of $\gamma < \gamma_{\mathrm{F}}$, we seek to determine the decay rate $\lambda_j(\gamma) < 0$ of each wave mode. Specifically, we must find λ_j and $\boldsymbol{x}_j(\gamma) \neq 0$ so that $\boldsymbol{M}(\lambda_j,\gamma)\boldsymbol{x}_j = \boldsymbol{0}$. Such a problem is computationally challenging owing to the nonlinear appearance of λ_j in Eq. (B13). Instead, we focus on the relevant and asymptotically tractable case of near-critical forcing, for which the vibrational acceleration γ is close to the critical vibrational forcing γ_j for the given eigenmode. For this section, we ignore modes satisfying $\gamma_j < 0$, which are strongly damped (and so fall outside of the regime of near-critical forcing).

We proceed by seeking an asymptotic expansion in terms of the parameter $\epsilon_j = (\gamma_j - \gamma)/g$, where $0 < \epsilon_j \ll 1$ for near-critical modes. Specifically, we posit

$$\lambda_j \sim \epsilon_j\lambda_{j,1} + O(\epsilon_j^2), \tag{B15a}$$

$$\boldsymbol{x}_j \sim \boldsymbol{x}_{j,0} + \epsilon_j\boldsymbol{x}_{j,1} + O(\epsilon_j^2), \tag{B15b}$$

where $\boldsymbol{x}_{j,0} \neq \boldsymbol{0}$ satisfies $\boldsymbol{M}(0,\gamma_j)\boldsymbol{x}_{j,0} = \boldsymbol{0}$. Upon substituting the asymptotic expansions (B15) and perturbation $\gamma = \gamma_j - g\epsilon_j$ into the equation $\boldsymbol{M}(\lambda_j,\gamma)\boldsymbol{x}_j = \boldsymbol{0}$, we Taylor expand the arguments of $\boldsymbol{M}$. After some algebra, we obtain

$$\lambda_{j,1}\boldsymbol{M}_\lambda(0,\gamma_j)\boldsymbol{x}_{j,0} - g\boldsymbol{M}_\gamma(0,\gamma_j)\boldsymbol{x}_{j,0} + \boldsymbol{M}(0,\gamma_j)\boldsymbol{x}_{j,1} = O(\epsilon_j),$$

where subscripts denote partial differentiation of the matrix $\boldsymbol{M}(\lambda,\gamma)$. By neglecting terms of size $O(\epsilon_j)$, we observe that $\boldsymbol{x}_{j,1}$ satisfies the linear system

$$\boldsymbol{M}(0,\gamma_j)\boldsymbol{x}_{j,1} = [g\boldsymbol{M}_\gamma(0,\gamma_j) - \lambda_{j,1}\boldsymbol{M}_\lambda(0,\gamma_j)]\boldsymbol{x}_{j,0}, \tag{B16}$$

where we recall that $\boldsymbol{M}(0,\gamma_j)$ is a singular matrix. By the Fredholm alternative theorem, there exists a solution for $\boldsymbol{x}_{j,1}$ when

$$\boldsymbol{z}_{j,0}^*[g\boldsymbol{M}_\gamma(0,\gamma_j) - \lambda_{j,1}\boldsymbol{M}_\lambda(0,\gamma_j)]\boldsymbol{x}_{j,0} = 0, \tag{B17}$$

where $\boldsymbol{z}_{j,0}$ is a left eigenvector of the singular matrix $\boldsymbol{M}(0,\gamma_j)$. Specifically, $\boldsymbol{z}_{j,0}$ satisfies $\boldsymbol{z}_{j,0}^*\boldsymbol{M}(0,\gamma_j) = \boldsymbol{0}$, where $*$ denotes the conjugate transpose. By rearranging Eq. (B17), we thus deduce that the leading-order decay rate $\lambda_{j,1} < 0$ is defined by the quotient

$$\lambda_{j,1} = \frac{g\boldsymbol{z}_{j,0}^*\boldsymbol{M}_\gamma(0,\gamma_j)\boldsymbol{x}_{j,0}}{\boldsymbol{z}_{j,0}^*\boldsymbol{M}_\lambda(0,\gamma_j)\boldsymbol{x}_{j,0}},$$

where $\boldsymbol{M}_\gamma(0,\gamma_j) = \frac{1}{2}(\boldsymbol{BA} - \boldsymbol{AB})$ and $\boldsymbol{M}_\lambda(0,\gamma_j) = -2\boldsymbol{A}$. Although one may, in principle, proceed to solve Eq. (B16) for the higher-order correction to the eigenmode, denoted $\boldsymbol{x}_{j,1}$, we find that the leading-order form $\boldsymbol{x}_j = \boldsymbol{x}_{j,0} + O(\epsilon_j)$ is satisfactory for our purposes. The growth rate may then be approximated by $\lambda_j \sim \lambda_{j,1}(\gamma_j - \gamma)/g$.

Finally, it remains to efficiently compute the left eigenvector $\boldsymbol{z}_{j,0}$. Using a similar formulation to Appendix B 3 b,

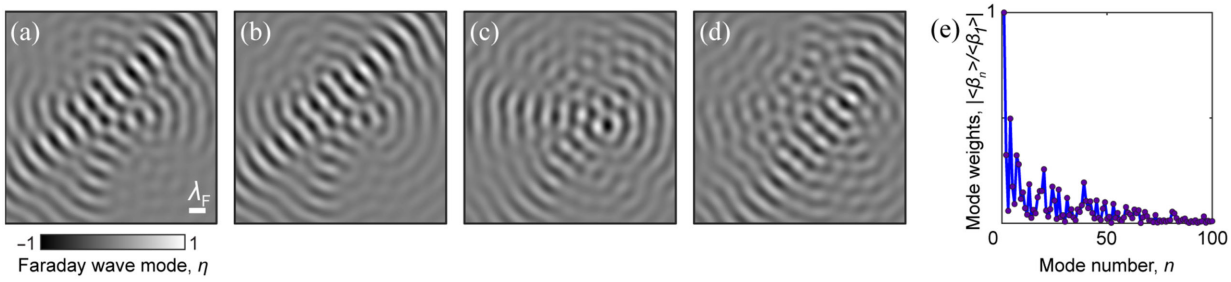

FIG. 6. Theoretical Faraday eigenmodes. Subcritical Faraday modes with the slowest decay rates computed theoretically (Appendix B 3). The critical thresholds are $\gamma/g =$ (a) 3.7648, (b) 3.7658, (c) 3.7828, and (d) 3.7852, respectively. For $\gamma/\gamma_F = 99.89\%$, the corresponding decay rates are $\lambda T_F =$ (a) −0.0016, (b) −0.0020, (c) −0.0084, and (d) −0.0093. Each eigenmode is normalized by its maximum value. (e) The absolute value of the mode weights, $|\langle\beta_n\rangle|$, normalized by that of the dominant mode, $|\langle\beta_1\rangle|$, for the modal composition of the mean wave field accompanying the probability density function in Fig. 9(c). The modes are ordered with decreasing proximity to the Faraday threshold, and their weightings decrease slowly (and nonuniformly) with the mode number n [Appendix B 4 b, Eq. (B23)].

we deduce that $z_{j,0}$ and γ_j satisfy the generalized left-eigenvector problem

$$z_{j,0}^* \mathcal{A} = \gamma_j z_{j,0}^* \mathcal{B}.$$

By postmultiplying by $\mathcal{A}^{-1}$ and taking the conjugate transpose of both sides, we deduce that $z_{j,0}$ is a right eigenvector of the matrix $(\mathcal{B}\mathcal{A}^{-1})^*$ with real eigenvalue γ_j^{-1}.

The first four Faraday modes (ordered with increasing $\gamma_j > 0$) are presented in Fig. 6. The first mode is the dominant Faraday mode and has the slowest decay rate for vibrational forcing just below the Faraday threshold. Notably, the predicted Faraday threshold $\gamma_F = 3.7648g$ is close to the estimation from simulations, $\gamma_F = 3.806g$ (Appendix D 1 a). The modes typically align across the diagonal of the cavity, with the direction selected by the relative wave excitation within the localization region. The first two modes are closely related by a phase shift and have very similar critical thresholds and decay rates.

4. Mean wave field

We proceed to consider the evolution of the pilot wave generated by successive droplet impacts, with a particular focus on the statistical convergence of the wave field according to the long-time average [43,44]

$$\langle\eta\rangle(\boldsymbol{x}) = \lim_{N\to\infty} \frac{1}{N} \sum_{n=0}^{N-1} \eta(\boldsymbol{x}, t_n).$$

Specifically, we use Floquet theory to determine an iterative map [63] (Appendix B 4 a) for the evolution of the near-critical Faraday modes $\boldsymbol{v}_F(t)$, which we then use to derive a formula for the contribution of Faraday modes to the time-averaged wave field (Appendix B 4 b). We then determine the analogous contribution of long waves, $\boldsymbol{v}_L(t)$, to the time-averaged wave field (Appendix B 4 c), which we couple with the contribution of Faraday modes to determine the predominant features of the mean wave field, $\langle\eta\rangle(\boldsymbol{x})$ (Appendix B 4 d).

a. Faraday modes: Iterative map

Between successive impacts, we use the linearly independent Floquet solutions [see Eq. (B10)] as a basis for $\boldsymbol{v}_F(t)$. During droplet flight, i.e., $t_n < t < t_{n+1}$, we may thus write

$$\boldsymbol{v}_F(t) = \sum_j c_j \boldsymbol{p}_j(t) e^{\lambda_j t},$$

where the c_j are arbitrary constants to be determined by the initial conditions and the sum is over all wave modes ($j = 1, \ldots, 2\mathcal{N}$). However, as we are primarily interested in the wave field at each impact (across which the free surface is continuous), we determine an iterative map for the value of the vector $\boldsymbol{v}_F(t_n^+)$, which represents the fluid variables just after each impact [43,63].

To determine the iterative map, we start by expressing

$$\boldsymbol{v}_F(t_n^+) = \sum_j \beta_{j,n} \boldsymbol{p}_j(t_n) \quad \text{for all } n, \tag{B18}$$

where we proceed to determine the evolution of the coefficients, $\beta_{j,n}$, between successive impacts. By exploiting the periodicity of $\boldsymbol{p}_j(t)$, we compute

$$\boldsymbol{v}_F(t_{n+1}^-) = \sum_j \beta_{j,n} e^{\lambda_j T_F} \boldsymbol{p}_j(t_n),$$

which we couple with the jump condition $[\boldsymbol{v}_F(t_{n+1})]_-^+ = -\boldsymbol{f}_{n+1}$ to obtain

$$\boldsymbol{v}_F(t_{n+1}^+) = \sum_j \beta_{j,n} e^{\lambda_j T_F} \boldsymbol{p}_j(t_n) - \boldsymbol{f}_{n+1}. \tag{B19}$$

To simplify notation, we define the matrix of periodic solutions $\boldsymbol{P} = [\boldsymbol{p}_1(t_n), \boldsymbol{p}_2(t_n), \ldots]$, the diagonal matrix $\boldsymbol{\Lambda}$

with diagonal elements $e^{\lambda_j T_F}$ (the Floquet multipliers), and the column vector $\boldsymbol{\beta}_n$ with elements $\beta_{j,n}$. By noting that Eqs. (B18) (with n replaced by $n+1$) and (B19) may be written as $\boldsymbol{v}_F(t_{n+1}^+) = \boldsymbol{P}\boldsymbol{\beta}_{n+1}$ and $\boldsymbol{v}_F(t_{n+1}^+) = \boldsymbol{P}\boldsymbol{\Lambda}\boldsymbol{\beta}_n - \boldsymbol{f}_{n+1}$, respectively, we eliminate $\boldsymbol{v}_F(t_{n+1}^+)$ to deduce the iterative map

$$\boldsymbol{P}\boldsymbol{\beta}_{n+1} = \boldsymbol{P}\boldsymbol{\Lambda}\boldsymbol{\beta}_n - \boldsymbol{f}_{n+1}. \tag{B20}$$

Finally, we use the linear independence of the periodic solutions $\boldsymbol{p}_j(t)$ to invert the matrix $\boldsymbol{P}$ in Eq. (B20), giving rise to the diagonal system

$$\boldsymbol{\beta}_{n+1} = \boldsymbol{\Lambda}\boldsymbol{\beta}_n - \boldsymbol{P}^{-1}\boldsymbol{f}_{n+1}. \tag{B21}$$

The matrix $\boldsymbol{\Lambda}$ encodes the damping of each wave mode between successive droplet impacts and may be regarded as the system's diagonalized fundamental matrix over one Faraday period [43,63]. The iterative map (B21) may be used for simulating and analyzing the dynamics of the pilot-wave system; in particular, we proceed to use this framework to connect the droplet's statistics to the accompanying mean wave field.

b. Contribution of Faraday modes

The contribution of Faraday modes to the time-averaged wave field may be found by computing

$$\langle\boldsymbol{\beta}\rangle = \lim_{N\to\infty}\frac{1}{N}\sum_{n=0}^{N-1}\boldsymbol{\beta}_n,$$

where $\boldsymbol{v}_F(t_n^+) = \boldsymbol{P}\boldsymbol{\beta}_n$ and we recall that η is continuous across each impact. We assume that the pilot-wave system (i) satisfies the ergodic hypothesis, which allows us to replace temporal averages with spatial averages, and (ii) exhibits a stationary probability distribution for the droplet position, denoted $p_s(\boldsymbol{x})$ [43,44]. The apparent validity of these assumptions has been justified from various experimental and numerical observations [34,43,44,65,66]. By applying the partial sum $N^{-1}\sum_{n=0}^{N-1}$ to Eq. (B21) and considering the limit as $N\to\infty$, we deduce that

$$\langle\boldsymbol{\beta}\rangle = \boldsymbol{\Lambda}\langle\boldsymbol{\beta}\rangle - \boldsymbol{P}^{-1}\iint_{\mathcal{D}} p_s(\boldsymbol{x})\boldsymbol{f}(\boldsymbol{x})\mathrm{d}\boldsymbol{x}. \tag{B22}$$

By substituting in the definition of $\boldsymbol{f}(\boldsymbol{x})$ [see Eq. (B7)] into Eq. (B22) and rearranging, we conclude that

$$\langle\boldsymbol{\beta}\rangle = -\frac{mgT_F}{\rho}(\boldsymbol{I}-\boldsymbol{\Lambda})^{-1}\boldsymbol{P}^{-1}\begin{pmatrix}\hat{\boldsymbol{p}}_s\\ \boldsymbol{0}\end{pmatrix}, \tag{B23}$$

where $\hat{\boldsymbol{p}}_s$ is a column vector (of length $\mathcal{N}$) with elements $\iint_{\mathcal{D}} p_s(\boldsymbol{x})e^{-i\boldsymbol{k}_j\cdot\boldsymbol{x}}\mathrm{d}\boldsymbol{x}$, corresponding to the discrete Fourier transform of the probability density function, $p_s(\boldsymbol{x})$, over the domain $\mathcal{D}$. Upon computing $\langle\boldsymbol{\beta}\rangle$, we may then determine the contribution of near-critical Faraday waves to the mean wave field from the product $\boldsymbol{P}\langle\boldsymbol{\beta}\rangle$.

c. Contribution of long waves

We proceed to develop an iterative map for the evolution of long waves, which we then use to determine the contribution of long waves to the mean wave field. During droplet flight, we deduce from Eq. (B8) that $\boldsymbol{v}_L(t)$ has linearly independent solutions

$$\boldsymbol{v}_{L,j}(t) = e^{\mu_j t}\boldsymbol{q}_j \quad \text{for } j = 1,\ldots,2\mathcal{N},$$

where the nonzero vector $\boldsymbol{q}_j$ and scalar μ_j satisfy the eigenvalue problem $\boldsymbol{A}\boldsymbol{q}_j = \mu_j\boldsymbol{q}_j$. We now determine an iterative map for $\boldsymbol{v}_L(t_n^+) = \boldsymbol{Q}\boldsymbol{\alpha}_n$ in terms of the matrix of eigenvectors $\boldsymbol{Q} = (\boldsymbol{q}_1, \boldsymbol{q}_2, \ldots)$ and the corresponding coefficients $\boldsymbol{\alpha}_n$. By following a framework similar to Appendix B 4 a, we deduce that the eigenmode coefficients $\boldsymbol{\alpha}_n$ evolve according to the iterative map

$$\boldsymbol{\alpha}_{n+1} = \boldsymbol{D}\boldsymbol{\alpha}_n - \boldsymbol{Q}^{-1}\boldsymbol{f}_{n+1},$$

where $\boldsymbol{D}$ is a diagonal matrix with diagonal elements $e^{\mu_j T_F}$. This map is analogous to the map for the evolution of the Faraday modes [Eq. (B21)]. Finally, under the assumptions of ergodicity and the existence of a stationary probability density function for the droplet position, we follow a framework similar to Appendix B 4 b to determine the contribution of long waves to the mean wave field. Analogous to Eq. (B23), we deduce that the time-averaged eigenmode coefficients

$$\langle\boldsymbol{\alpha}\rangle = \lim_{N\to\infty}\frac{1}{N}\sum_{n=0}^{N-1}\boldsymbol{\alpha}_n$$

satisfy

$$\langle\boldsymbol{\alpha}\rangle = -\frac{mgT_F}{\rho}(\boldsymbol{I}-\boldsymbol{D})^{-1}\boldsymbol{Q}^{-1}\begin{pmatrix}\hat{\boldsymbol{p}}_s\\ \boldsymbol{0}\end{pmatrix}. \tag{B24}$$

d. Mean wave field structure

We determine the structure of the mean wave field using the approximate superposition of the contributions of Faraday modes and long waves, namely, $\langle\eta\rangle \approx \langle\eta_F\rangle + \langle\eta_L\rangle$. We consider the contribution of different Faraday modes to $\langle\eta_F\rangle$ [using $\langle\boldsymbol{\beta}\rangle$ defined in Eq. (B23)], where we order the modes so that $\gamma_F = \gamma_1 \le \gamma_2 \le \gamma_3 \le \cdots$ (and we neglect modes with critical threshold $\gamma_j < 0$, which are strongly damped). In particular, we approximate $\boldsymbol{p}_j(t)$ by neglecting higher harmonics in the wave oscillation [see Eq. (B11)] and consider $\boldsymbol{x}_j \sim \boldsymbol{x}_{j,0}$ and $\boldsymbol{y}_j \sim \boldsymbol{y}_{j,0}$; likewise, we approximate the decay rates using the asymptotic form $\lambda_j \sim \lambda_{j,1}(\gamma_j - \gamma)/g$. We also normalize each vector $\boldsymbol{p}_j(t_n)$ so that $\|\boldsymbol{p}_j(t_n)\| = 1$.

Two factors control the relative contribution of each Faraday mode to the mean wave field: (i) the proximity of the vibrational forcing to the mode's critical threshold and (ii) the size of the projection of the probability density function, $p_s(\boldsymbol{x})$, onto the Faraday mode. Owing to the complex structure of the Faraday wave field over the disordered topography, we find that $\langle \eta_F \rangle$ may not be simply approximated by a small number of Faraday modes, with the mode weightings decreasing slowly with the mode number [see Fig. 6(e)]. Finally, we compute $\langle \eta_L \rangle$ [using $\langle \boldsymbol{\alpha} \rangle$ defined in Eq. (B24)] with all $2\mathcal{N}$ eigenmodes included, with the results presented in Fig. 4(d) in the main text.

APPENDIX C: QUANTUM LOCALIZATION

1. Schrödinger's equation

We consider the time-dependent Schrödinger's equation in a 2D square domain Ω of width L with Dirichlet boundary conditions along the border, $\partial\Omega$. We nondimensionalize the problem using $x_c = L$, $t_c = mL^2/\hbar$, and $V_c = \hbar^2/mL^2$ as the characteristic scales for length, time, and energy, respectively. Here, m is the mass and $\hbar$ the reduced Planck constant. In dimensionless form, the Schrödinger problem for the wave function $\Psi(\boldsymbol{x}, t)$, thus, becomes

$$\mathrm{i}\frac{\partial \Psi}{\partial t} = -\frac{1}{2}\nabla^2\Psi + V(\boldsymbol{x})\Psi, \tag{C1}$$

$$\Psi = 0 \quad \text{on } \partial\Omega, \tag{C2}$$

$$|\Psi(\boldsymbol{x}, 0)|^2 = C_0 \exp\left(-\frac{|\boldsymbol{x}|^2}{2\sigma^2}\right) \quad \text{on } \Omega, \tag{C3}$$

where $V(\boldsymbol{x})$ is the dimensionless potential and Ω a square domain of width 1. The problem is initialized with a purely real Gaussian wave packet with standard deviation σ that is normalized by C_0 such that the probably density function integrates to one: $\iint_\Omega |\Psi(\boldsymbol{x}, 0)|^2 \mathrm{d}S = 1$.

Seeking separable solutions of the form $\Psi(\boldsymbol{x}, t) = \varphi(t)\psi(\boldsymbol{x})$, the general solution may written in the standard way as

$$\Psi(\boldsymbol{x}, t) = \sum_{n=1}^{\infty} c_n \mathrm{e}^{-\mathrm{i}E_n t}\psi_n(\boldsymbol{x}), \tag{C4}$$

where the energies E_n and normal modes $\psi_n(\boldsymbol{x})$ are the eigenvalues and eigenfunctions of the time-independent Schrödinger equation

$$\mathcal{H}(\boldsymbol{x})\psi \equiv -\frac{1}{2}\nabla^2\psi + V(\boldsymbol{x})\psi = E\psi, \tag{C5}$$

with the same boundary conditions. Here, $\mathcal{H}(\boldsymbol{x})$ represents the quantum Hamiltonian operator. The total energy may be computed through the integral $E = \iint_\Omega \Psi^* \mathcal{H}(\boldsymbol{x})\Psi \mathrm{d}S$, where the asterisk denotes the complex conjugate. The evolution of the particle's mean-squared displacement, or second moment of the probability density function $|\Psi|^2$, is $\langle r^2(t) \rangle = \iint_\Omega |\Psi|^2 r^2 \mathrm{d}S$, where $r = |\boldsymbol{x}|$ is the radial coordinate with respect to the origin of the coordinate system located at the center of the domain.

2. Anderson localization

Consider a classical particle evolving according to $m\ddot{\boldsymbol{x}}_p(t) = -\nabla V(\boldsymbol{x}_p)$, where $V(\boldsymbol{x})$ is a random potential. The particle is subject to weak disorder when the total energy $E = \frac{1}{2}m|\dot{\boldsymbol{x}}_p|^2 + V(\boldsymbol{x}_p)$ is larger than the characteristic potential energy of the background, V_0, i.e., $E/V_0 > 1$. The particle, thus, has sufficient energy to explore the entire potential, the process during which the particle's trajectory becomes deflected in random directions, leading to diffusive motion in the long-time limit in two (or higher) dimensions [2].

Anderson localization describes the fundamentally different behavior of quantum particles in the equivalent situation. Owing to their wave-particle duality, quantum particles exhibit a remarkable phenomenon wherein even a weak disordered potential causes them to spontaneously halt, in stark contrast to classical expectations [39]. This absence of diffusion is observed for a sufficient degree of randomness; the emergent eigenmodes become exponentially localized (Fig. 7) even when the total energy of the particle is larger than the potential energy of the heterogeneous background [29]. In the quantum regime, the conditions for weak disorder [39] are $E_\zeta E/V_0^2 > 1$ and $E_\zeta/V_0 > 1$, where $E_\zeta = 1/\zeta^2$ is the dimensionless energy associated to the potential's correlation length ζ. The correlation length ζ and characteristic magnitude of the random potential, V_0, are computed through the average correlation function $\langle V(\boldsymbol{x}')V(\boldsymbol{x}' + \boldsymbol{x}) \rangle = V_0^2 f(r)$, where $f(r)$ is a function with $\max f = 1$ at the origin [39]. For our potential composed of square tiles of constant width and random height, $f(r)$ decays linearly near the origin. We thus approximate $f(r) \approx -V_0^2(r/\zeta - 1)$ in the interval $0 \le r \le W$ to compute the correlation length ζ. As expected for our random potential, we find that the correlation length roughly corresponds to the tile width, $\zeta \approx W$, in all realizations.

Observation of Anderson localization is also dependent on the system dimension. The scaling theory of localization specifies that all states become localized in 2D while an energy threshold, or "mobility edge," separates localized and nonlocalized states in higher dimensions [67]. Moreover, the quantum system must be tuned into a scattering regimen for which the product kl should be of the order of unity in 2D (and smaller in higher dimensions), where k is the de Broglie wave number and l the mean free path [39]. Assuming that the mean free path is roughly

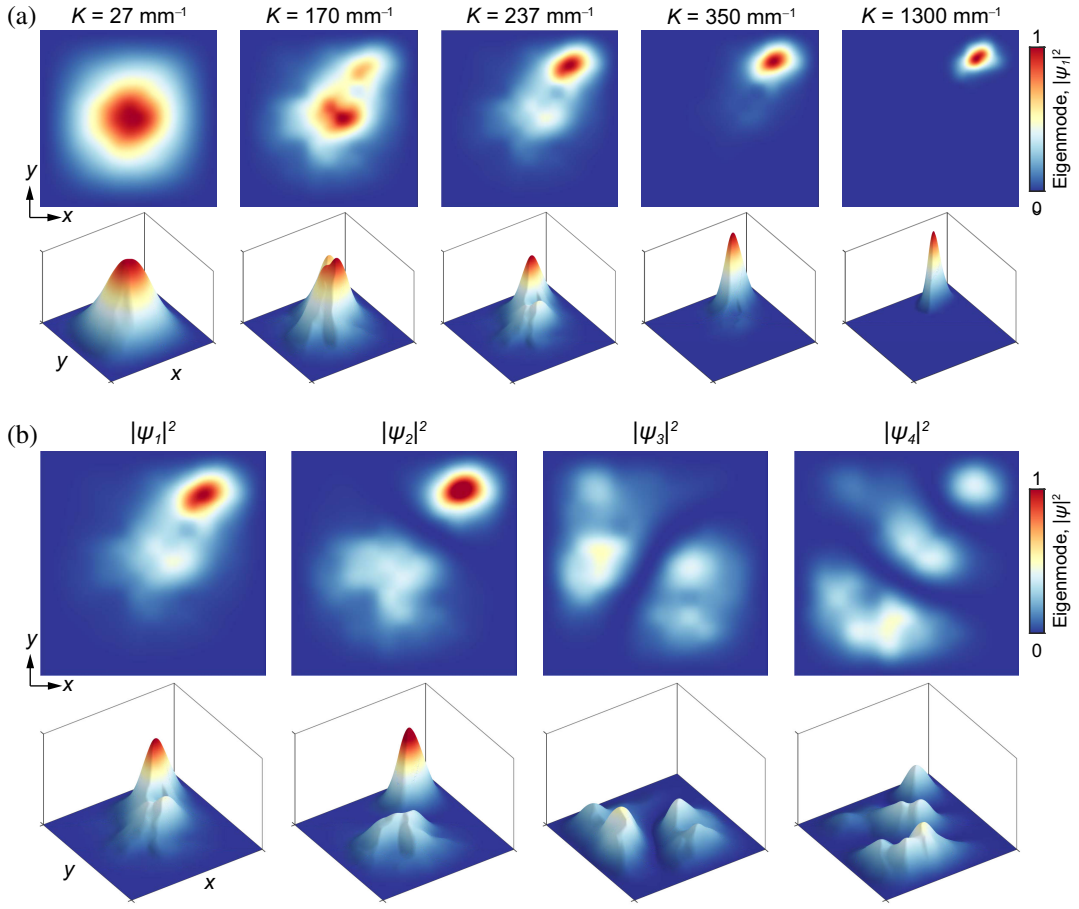

FIG. 7. Eigenfunctions of Schrödinger's equation. (a) Ground states $|\Psi_1|^2$ arising from Schrödinger's equation (C5) with a potential of the same form as the walker's bottom topography (C6) for different values of rescaling constant K. The associated energies are listed in Table I. (b) First four eigenfunctions for the potential with $K = 237$ mm^{-1}, whose dimensionless energies are $E_1 = 76.5$, $E_2 = 86.9$, $E_3 = 102.2$, and $E_4 = 107.4$, respectively. The first eigenfunction, Ψ_1, is the mode presented in Fig. 1.

comparable to the tile width, $l \approx W$, we obtain $kl = 0.9$ for the simulations presented in Fig. 2.

a. Localized eigenfunctions

For walking droplets above variable bottom topography, deeper and shallower areas act as regions of lower and higher potential, respectively [35,68]. To investigate qualitatively the quantum eigenmodes for a random medium of the same form as the walker's bottom topography in the experiment, we thus define the dimensionless potential for the Schrödinger problem (C5) as

$$V(\boldsymbol{x}) = -K(H(\boldsymbol{x}) - \max H(\boldsymbol{x})), \tag{C6}$$

where $K = \kappa/V_c$ and $H(\boldsymbol{x})$ have dimensions of $1/\text{length}$ and length, respectively. Here, $H(\boldsymbol{x})$ is the random liquid depth distribution used in the experiments and κ the dimensional scaling constant presented in the main text, which has dimensions of energy over length. We note that Eq. (C6) is equivalent to

$$V(\boldsymbol{x}) = K\Delta\hat{H}(\boldsymbol{x}), \tag{C7}$$

where $\Delta\hat{H}(\boldsymbol{x})$ are the random heights drawn from the uniform distribution in the interval [0, 0.6] mm.

We discretize the time-independent Schrödinger equation (C5) using a finite-difference method with a central difference for the space derivatives and Dirichlet conditions along the border. In matrix form, the problem thus becomes $\boldsymbol{M}\boldsymbol{\psi}_n = E_n\boldsymbol{\psi}_n$ (for $n = 1, 2, \ldots$), where the vector $\boldsymbol{\psi}_n$ is the discretized eigenfunction with energy E_n and $\boldsymbol{M}$ is a matrix of coefficients. We discretize the domain, which is composed of 13×13 tiles, using 256×256 points (approximately 20 points per tile) and verify that using 512×512 points (approximately 39 points per tile) yields virtually the same results. The emergent eigenfunctions for several values of the rescaling constant K are presented in Fig. 7(a), and the associated energies are listed in Table I. The mode presented in the main text (Fig. 1) corresponds to $K = 237$ mm^{-1}. Higher-energy modes for the same value of K are presented in Fig. 7(b).

TABLE I. Dimensionless energies and energy ratios for the first eigenfunction (ground state E_1) of the time-independent Schrödinger equation (C5) shown in Fig. 7(a) for different values of the scaling factor K in the random potential (C6).

K (mm^{-1})	V_0	E_1	E_ζ	$E_\zeta E_1/V_0^2$	E_ζ/V_0
27	6.16	18.3	135.6	65.3	22.0
170	38.8	59.7	135.6	5.38	3.50
237	54.1	76.5	135.6	3.55	2.51
350	79.8	98.5	135.6	2.09	1.70
1300	296.6	192.0	135.6	0.30	0.46

b. Absence of diffusion

To demonstrate the absence of diffusion of quantum particles in disordered media, we perform simulations of the time-dependent Schrödinger's equation (C1) in a domain larger than that described in Fig. 1. Specifically, we increase the number of tiles to 37×37 and readjust the rescaling constant $K = 3200$ mm^{-1} in Eq. (C7) to obtain energy ratios similar to those corresponding to the eigenmode presented in Fig. 1. We replace the regularly spaced pillars, which do not play a significant role, with tiles of a random height drawn from the same uniform distribution. We average over 20 random realizations of the heterogeneous media. To facilitate the averaging, for each random realization, we shift the potential in the xy plane so that the peak of the ground state is located at the center of the domain. For the initial Gaussian wave packet (C3), we select a dispersion of $\sigma = 1/(12\sqrt{2})$, and the normalization constant is $C_0 = 2.114 \times 10^{-3}$. The resulting average energy ratios are $E_\zeta E/V_0^2 = 3.47 \pm 0.30$ and $E_\zeta/V_0 = 2.18 \pm 0.07$, where the interval represents the standard deviation and E is the total energy. We integrate Schrödinger's equation (C1) numerically using the Crank-Nicolson scheme to advance time. For the simulations presented in the main text, we use a spatial resolution of $N \times N = 222 \times 222$ points (approximately six points per tile) and a temporal resolution of $\Delta t = 1/(2N^2)$. We perform numerical tests with other resolutions (four, five, seven, and eight points per tile) to ensure that our results are independent of the spatiotemporal discretization. As the resolution is increased, the final MSD converges to the same value. For the resolution selected for the final simulations, the MSD differs by only 0.32% with respect to that of the highest resolution. The temporal evolution of average wave packet and MSD are presented in Fig. 2. The wave function effectively freezes, i.e., the MSD saturates, well before reaching the maximum allowed by the size of the domain, specifically, $(L/2)^2 = 0.25$.

APPENDIX D: SIMULATIONS

1. Walking droplets

We perform numerical simulations of walking droplets using the pilot-wave model of Faria [42], which couples a variable-topography wave model (B1) with the trajectory equation [32] for the droplet (B3), as described in Appendix B 1. Between droplet impacts, which are modeled as delta functions in time and space, the droplet evolution (B3) is solved analytically, while the wave model (B1) is solved numerically in a doubly periodic square domain using a pseudospectral method in space and a fourth-order Runge-Kutta scheme for the time integration [42]. Each droplet impact is resolved analytically by applying appropriate jump conditions [42,63] in the droplet's velocity (B4) and fluid velocity potential (B7).

a. Faraday threshold

The Faraday threshold γ_F is the critical vibrational acceleration γ above which perturbations in the bath's fluid rest state grow. The growth is exponential in time for $\gamma > \gamma_F$, with exponential decay for $\gamma < \gamma_F$ [see Appendix B 3 a and Fig. 8(a)]. Near the Faraday threshold, we expect the wave growth or decay rate $\lambda(\gamma)$ to satisfy $\lambda(\gamma) \sim \lambda_0(\gamma - \gamma_F)$, with $\lambda_0 > 0$ so that $\lambda > 0$ for $\gamma > \gamma_F$ and $\lambda < 0$ for $\gamma < \gamma_F$ (see Appendix B 3 c). Consequently, we may obtain a numerical estimation of the Faraday threshold for each realization of the random topography by exciting a disturbance in the wave surface and measuring the wave growth or decay for different acceleration values γ.

Specifically, we characterize the evolution of the free surface in terms of the L_2 norm of the free surface, $\|\eta\|$, computed over the spatial domain. For a given value of γ, we initialize each simulation by exciting a zeroth-order Bessel function in the deepest region of the topography and recording $\|\eta\|$ over 1000 Faraday periods. We then numerically estimate the long-time exponential growth or decay rate $\lambda(\gamma)$ [Fig. 8(a)]. Upon repeating this process for several values of γ close to the instability threshold, we estimate the parameters λ_0 and $c = -\lambda_0\gamma_F$ with a linear least-squares fit, $\lambda \sim c + \lambda_0\gamma$ [Fig. 8(b)]. Upon computing c and λ_0, the Faraday threshold is then $\gamma_F = -c/\lambda_0$.

b. Simulation of the experiments

To test whether the pilot-wave model (B1)–(B3) captures the walker localization observed in experiments, we integrate the governing equations numerically using a square domain of size $L \times L = 19\lambda_F \times 19\lambda_F$, in which the random topography of size $13\lambda_F \times 13\lambda_F$ is surrounded by a damper (i.e., a shallow fluid layer) of width $3\lambda_F$. Preliminary tests show that the influence of the random topography on the droplet dynamics in the simulations is weaker than that in the experiments. Maintaining the same base depth as in the experiments, we thus rescale the random fluid depths in the simulations as $H(\boldsymbol{x}) = H_0 - (5/3)\Delta H(\boldsymbol{x})$, including the height of the damper [Fig. 14(a)]. The problem is discretized using a spatial resolution of $N \times N = 204 \times 204$ points (approximately 11 points per wavelength) and a temporal resolution of $\Delta t = T_F L/(10N\lambda_F)$, where $T_F = 2/f$ is the Faraday period. Numerical tests are performed to ensure

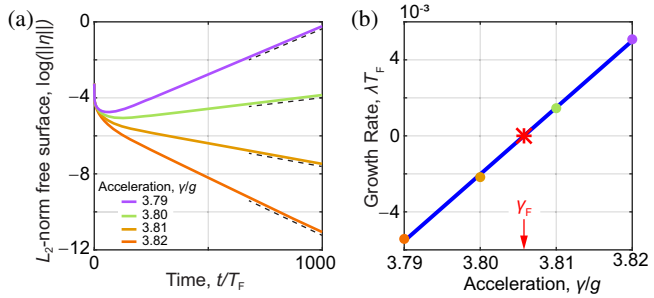

FIG. 8. Numerical estimation of the Faraday threshold. (a) Temporal evolution of the L_2 norm of the free surface, $\|\eta\|$, for different vibrational forcings γ. (b) Calculation of the Faraday threshold γ_F by applying a linear least-squares fit to the time exponential growth or decay rates, λ.

that the spatiotemporal resolution is adequate to render discretization-independent results (see Appendix D 1 j). We also perform tests with different widths of the wave damper to ensure that the periodic boundary conditions had no influence of the emergent statistics (see Appendix D 1 f).

The fluid properties and droplet radius are the same as in the experiments. The effective kinematic viscosity $\nu_e = 0.828\nu$ is chosen to match the experimental stability threshold γ_F [42,61]. The simulations are performed at $\gamma/\gamma_F = 99.89\%$, where $\gamma_F = 3.806g$ is the numerical threshold. We observe that the strength of the droplet localization is significantly influenced by the coefficient of restitution, which we set to $c_4 = 0.05$. We note that this value is lower than the typical values considered in the literature, $0.13 \leq c_4 \leq 0.33$ [32,61]. We tune the impact phase $\theta_I = 1.418\pi$rad to match the average speed in the simulations to that in the experiments. We simulate 36 walkers initialized with random conditions, each for 21 000 impacts or Faraday periods T_F. The simulations thus yield a total of 756 000 impacts, matching the duration of our experiments. The droplet position is saved at each impact. We also confirm the ergodicity of the system (see Appendix D 1 h).

The results of our simulations are presented in Fig. 9(c). The position histogram features localized statistics that agree well with the experiments. We note that the average speed map depicts some differences with respect to the experimental map, which indicates that the walker localization is not significantly influenced by the details of the instantaneous speed. Indeed, comparing the speed histograms reveals a broader distribution in the simulations [Fig. 10(a)]. The differences may be rooted in the simplifying assumptions adopted for the derivation of theoretical pilot-wave model (B1)–(B3), including the modeling of the droplet bounces as point impacts and the prescription of purely subharmonic vertical dynamics. For example, we observe in experiments that occasionally the walker experiences chaotic changes in its vertical phase near the localization region. More subtle phase shifts may also potentially be induced by random wave reflections from topographical features, which can alter the wave amplitude at the droplet's position and, thus, its bouncing phase. While these effects, which are not accounted for in our simulations, may contribute to some differences in the speed distributions, the fact that the simplified model captures the walker localization suggests that these are unessential details.

We also compare the curvature of the walker trajectories in experiments and simulations. Notably, the preferred radii observed in the experiments are also apparent in the simulations [Fig. 10(b)]. To demonstrate that the preferred radii occur near the localization region, where the droplet executes many loops, we segment the droplet trajectories according to the local radius of curvature into two intervals, $0.30 \leq r/\lambda_F \leq 0.56$ and $0.67 \leq r/\lambda_F \leq 1$, containing the preferred radii [Fig. 10(c)]. By computing the position histogram for each segment, we observe that the loops with preferred radii indeed occur predominately near the localization region [Figs. 10(d) and 10(e)].

c. Wave field

To rationalize the mechanism responsible for the walker localization, we present a series of wave-mediated interactions between the droplet and submerged topography in Fig. 3. Experimentally, the wave field is captured using the semireflective mirror setup described in Appendix A 1. The video recording is strobed at the Faraday frequency (35 frames per second), and the acquisition phase (relative to the external driving) is tuned to record the waves near their maximum amplitude. The simulated wave field given by the quasipotential model (B1) is similarly saved with the Faraday frequency near its maximum amplitude, which roughly corresponds to a phase 26% of the Faraday period after each impact.

To illustrate further the role of the memory, we compare the wave field at high memory $\gamma/\gamma_F = 99\%$ (Fig. 3) and low memory $\gamma/\gamma_F = 83\%$ (Fig. 11), using simulations, which allow us to maintain the same walker speed by readjusting the impact phase. At low memory, the waves decay significantly faster in time. The resulting walker wave field is, thus, less extensive and more weakly influenced by the topography (Fig. 11). As the memory decreases, the force on the walker, thus, becomes more local (i.e., less sensitive to the prior path or spatially distant features), approaching the behavior of a "waveless" particle (see Appendix D 2) whose evolution is purely local (i.e., the force acting on the particle depends entirely on its current position).

d. Influence of pillars

To demonstrate that the inclusion of regularly spaced pillars [tiles with the same height above the base level in Fig. 1(c)] plays no significant role in the localization problem, we repeat the simulations described in Appendix D 1 b without them. Specifically, we make the height of each pillar random according to the same uniform

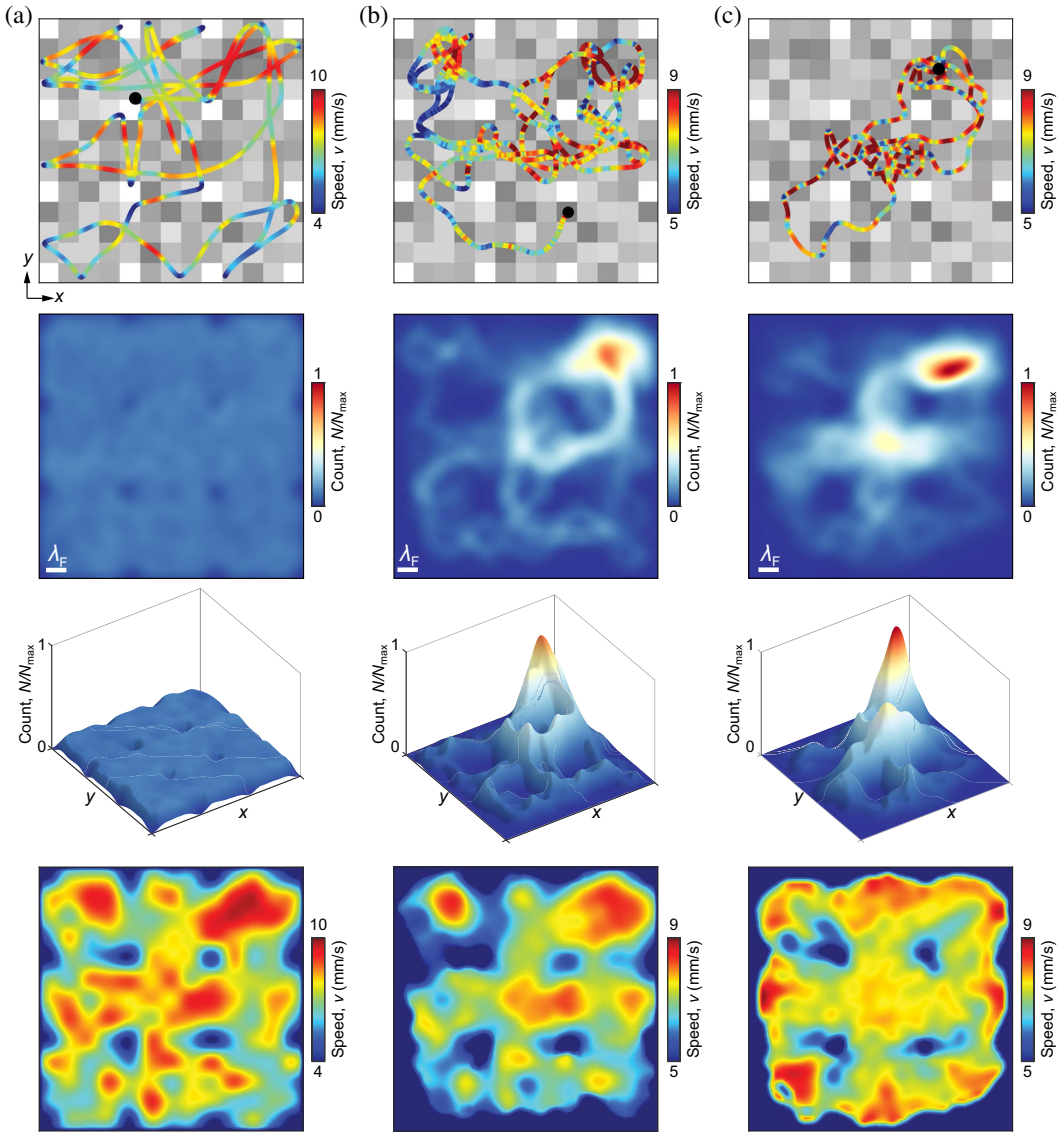

FIG. 9. Emergent localized statistics in the walker system. Comparison of the speed-colored trajectory (first row), position histogram (second and third rows), and average speed map (fourth row) for (a) a waveless particle (see Appendix D 2) and a walker according to (b) experiments (see Appendix A) and (c) simulations (see Appendix D 1). The position histograms $N(\boldsymbol{x})$ (computed using three bins per wavelength in each direction) are first normalized such that $\iint_\Omega N(\boldsymbol{x})\mathrm{d}S = 1$ and later rescaled by the maximum of the three histograms, $N_{\max}$. The average speed maps are computed using a 78×78 regular grid and a Gaussian-weighted average, with standard deviation $\sigma = \lambda_F/4$, applied to data points within $\lambda_F/4$ distance away from each grid point.

distribution used for the rest of the tiles. The height of the remaining tiles is maintained as before. The resulting submerged topography is presented in Fig. 12(a). The vibrational acceleration is readjusted to maintain the same memory γ/γ_F, with the new Faraday threshold being $\gamma_F = 3.783g$. We readjust the impact phase, $\theta_I = 1.419\pi$rad, to recover the same average speed. The emergent position histogram is presented in Fig. 12(b), which features localized statistics in the same region as in the case with pillars shown in Fig. 9(c).

To further demonstrate that the localized statistics are caused by the random topography, we also repeat the simulations with a topography that includes only the regularly spaced pillars. We, thus, set the depth of the fluid for the rest of the tiles to be the same as the base depth H_0 [Fig. 12(c)]. The new Faraday threshold is $\gamma_F = 3.825g$, and the impact phase is reset to its original value $\theta_I = 1.418\pi$rad. Without randomness, the emergent histogram shows no localization [Fig. 12(d)]. The emergent curvature distributions are presented in Fig. 12(e), which illustrates that the experimental topography with disorder between the pillars is an intermediate configuration between the regular topography with pillars and the fully disordered topography.

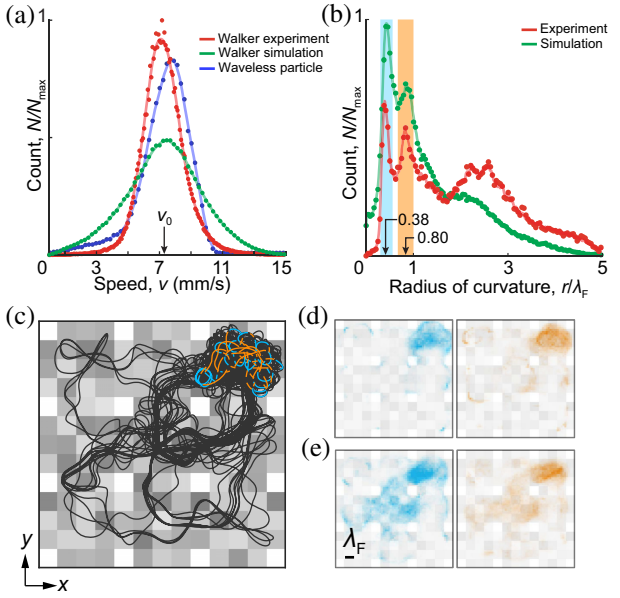

FIG. 10. Walker dynamics in experiments and simulations. Histograms of the instantaneous (a) droplet speed and (b) radius of curvature of the droplet trajectory. Each histogram $N(s)$ is normalized such that $\int_{-\infty}^{+\infty} N(s)\mathrm{d}s = 1$ and later rescaled by the maximum of the histograms, $N_{\max}$. Preferred radii of curvature around $r/\lambda_F \sim 0.38$ and 0.80 arise in both experiments and simulations. (c) To examine if there is a spatial correlation between the preferred radii and the localized statistics, we segment the droplet trajectory according to the local radius of curvature into two intervals, $0.30 \leq r/\lambda_F \leq 0.56$ [blue area in (b)] and $0.67 \leq r/\lambda_F \leq 1$ [orange area in (b)], containing the preferred radii. By computing the spatial histograms of the segmented trajectories for the (d) experiments and (e) simulations, we observe that the loops with preferred radii mainly occur in the localization region.

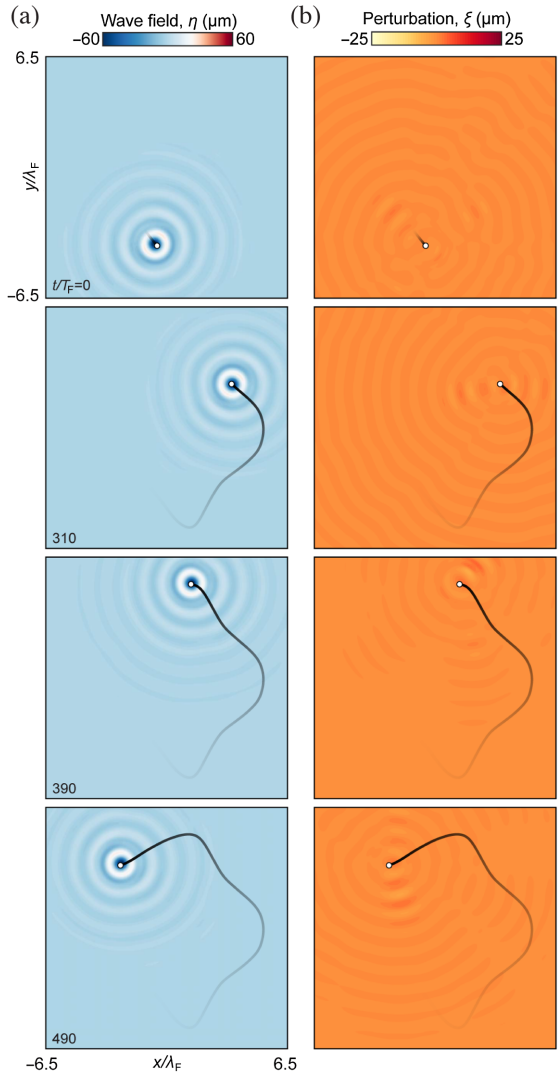

FIG. 11. Walker wave field at low memory. Repeating the simulations described in Fig. 3 at low memory, $\gamma/\gamma_F = 83.0\%$, reveals (a) a less extensive and more circularly symmetric wave field and (b) significantly weaker topography-induced wave perturbations. Thus, the influence of the submerged topography on the walker dynamics diminishes as the memory is reduced. In this simulations, the average walker speed is maintained the same as in Fig. 3 by readjusting the impact phase, $\theta_I = 1.367\pi$rad.

e. Role of disorder

To examine how disorder influences the formation of localized statistics in walking droplets, we conduct a series of simulations similar to those described in Appendix D 1 b, varying the degree of disorder in the submerged topography. Having shown that the pillars are not relevant for localization in Appendix D 1 d, we take the configuration depicted in Fig. 12(a) as the basis for this exploration. We then progressively reduce the level of disorder by randomly selecting a percentage of tiles and setting their depth equal to the base depth [Fig. 13(a)]. A secondary localization peak appears while the degree of disorder is relatively high; however, any indications of localization vanish when roughly half of the topography becomes ordered [Fig. 13(b)]. Furthermore, we perform an additional set of simulations wherein disorder is preserved exclusively in the region where localization had been observed with a completely random topography, setting the depth elsewhere in the bath equal to the base depth [Fig. 13(c)]. Despite the disordered region now being the deepest area in the domain, the localization disappears from the position histogram [Fig. 13(d)]. Comprehensive tests are performed to ensure that these results are independent of the initial conditions. These results, thus, indicate a nontrivial relationship between disorder and long-range effects in the emergence of localization with walking droplets.

f. Wave damper

We perform a series of simulations to investigate the influence of the wave damper surrounding the heterogeneous region. The submerged topography used for the reference simulation described in Appendix D 1 b is

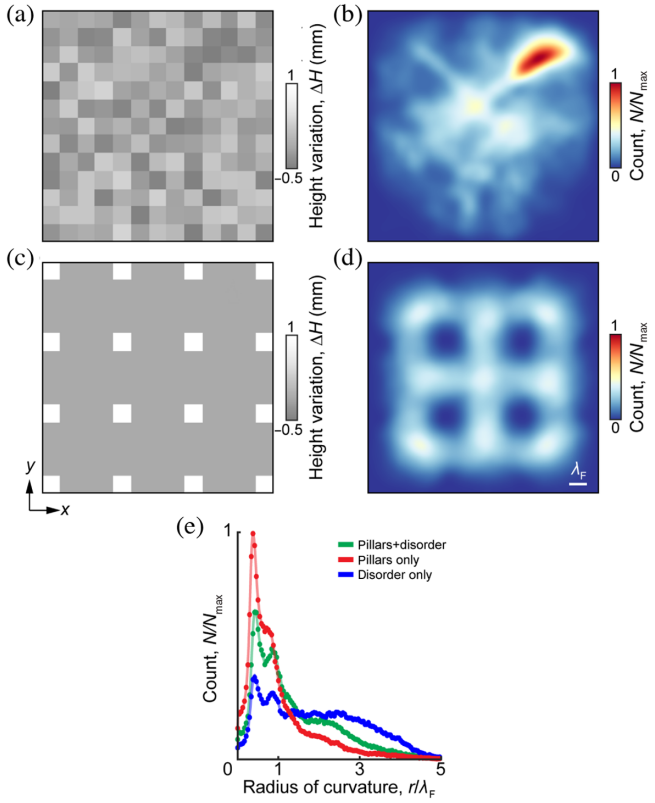

FIG. 12. Walker statistics in domains without regularly spaced pillars or disorder. Walker simulations with (a) a fully disordered submerged topography result in localized statistics as shown by (b) the droplet's position histogram. If the topography is ordered and includes only regularly spaced pillars (c), the position histogram remains symmetric (d). (e) Comparison of the curvature distributions.

presented in Fig. 14(a), for which the damper has a width of $3\lambda_F$ (the effective width of the damper is $6\lambda_F$ due to the periodic boundary conditions). To ensure that the waves are adequately damped above the border, we repeat the simulation with a damper twice as wide, as shown in

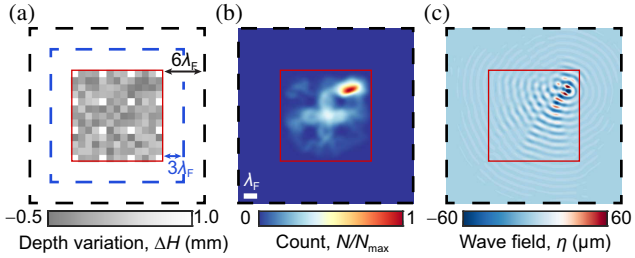

FIG. 14. Influence of the wave damper in the walker simulations. (a) Rescaled height about the base depth, $H_0 = 1.85$ mm, of the submerged topography used in the simulations described in Appendix D 1 b. The heterogeneous region is surrounded by a wave damper of width $3\lambda_F$, which is not shown in previous figures. Dashed lines denote the domain boundary along which periodic boundary conditions are prescribed. Simulations with a wider border, $6\lambda_F$, result in the same position histogram (b). (c) Visualization of the walker wave field demonstrates that the waves are indeed adequately damped above the border before they may reappear in the domain of interest due to the periodic boundary conditions. The wave field is shown at its maximum amplitude (Appendix D 1 c).

Fig. 14(a). We recompute the Faraday threshold γ_F to ensure that the prescribed memory γ/γ_F is the same as in the reference case. Our simulations with the wider damper yield virtually the same position histogram [Fig. 14(b)]. Moreover, we visualize the walker wave field to check that the waves are indeed damped above the border, thereby not "wrapping around" the periodic domain [Fig. 14(c)]. Our tests, thus, demonstrate that the wave damper is appropriate to ensure that the periodic boundary conditions in our simulations do not influence the walker dynamics.

g. Absence of diffusion

To demonstrate how the localized position statistics may lead to an absence of diffusion in the walker system, we perform simulations of walking droplets in domains larger than those accessible experimentally. Specifically, we

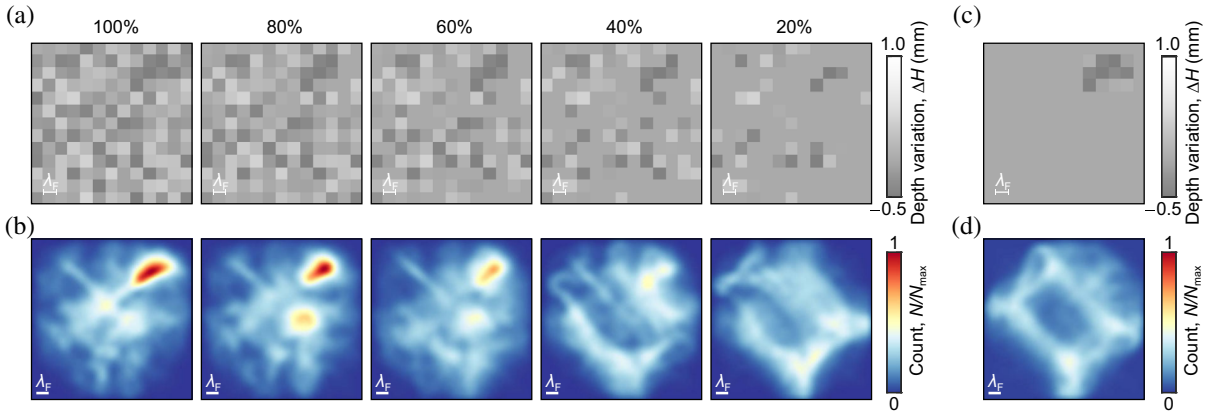

FIG. 13. Influence of disorder. Walker simulations with (a) a decreasing percentage of randomly selected tiles with heterogeneous heights along with (b) the resulting position histograms. (c) A specific configuration wherein disorder is retained solely in the region where localization emerges with a completely random topography, along with (d) its position histogram, which does not exhibit localization.

consider eight different random realizations of the potential in a domain with 36×36 tiles of the same width as in the experiments. Each realization is explored by 400 walkers for 2×10^4 bounces. The base depth is tuned to $H_0 = 1.45$ mm. The regularly spaced pillars from the experiment are excluded; the heights about the base depth of all the tiles are drawn from a rescaled distribution $H(\boldsymbol{x}) = H_0 - (4/3)\Delta H(\boldsymbol{x})$, chosen to show the full transition from diffusion to localization when sweeping in memory. We also remove the wave damper. Guided by preliminary simulations, we shift the random patterns on the xy plane to center the localization region on the computation domain and so facilitate the spatial averaging of the position histograms. The problem is solved numerically using approximately seven points per wavelength and temporal resolution as in the simulations of the experiments (see Appendix D 1 b). Each realization of the topography yields a slightly different Faraday threshold, which on average is $\gamma_F = 3.880g \pm 0.005g$, where the interval represents the standard deviation. Repeating the simulations at six different memories ($\gamma/\gamma_F = 77\%, 86\%, 90\%, 94\%$, and 97%) requires readjusting the impact phase with fine-tuned changes specific to each topography ($\theta_I/\pi = 1.340 \pm 0.001$, 1.392 ± 0.001, 1.408 ± 0.001, 1.421 ± 0.002, and 1.429 ± 0.002 rad, respectively) to yield the same average speed, $v_0 = 5.13 \pm 0.15$ mm s^{-1}. The results of these simulations are presented in Fig. 2 in the main text. The trajectories are unwrapped due to crossings of the periodic domain. At high memory, the crossings are very infrequent due to the walker localization. At low memory, the walkers cross the domain frequently, which materializes in the linear dependence on time of the MSD. This behavior is rationalized through the diminished influence of the submerged topography on the wave field, which is less extensive and decays quickly in time, making the walker behavior approach that of a waveless particle (see Appendix D 1 c, Fig. 11).

h. Ergodicity

In order to establish the ergodicity of walker localization, we conduct a comparison between statistical results derived from a substantial number of relatively short simulations and those obtained from a few extended simulations. We recall that the histogram presented in Fig. 9(c) is the result of simulating 36 randomly initialized walkers, each integrated over 21 000 Faraday periods (see Appendix D 1 b). We compare the results to those obtained from one walker, simulated up to 189 000 Faraday periods, and four walkers, each simulated up to 189 000 Faraday periods. The emergent position histograms are virtually the same (Fig. 15).

i. Base depth, droplet speed, and tile width

We perform tests to understand the role of the base depth H_0, walker average speed v_0, and tile width W. Reducing the base depth increases the influence of the submerged topography on the walker dynamics. Specifically, as the liquid layer becomes shallower, the random topography dominates more strongly the walker dynamics. The droplet, thus, explores a smaller fraction of the domain, thereby giving rise to a more pronounced peak than in the position histogram. In the opposite limit, as the layer depth increases, the heterogeneous topography distorts the droplet motion less and eventually becomes imperceptible in the deep-fluid limit $H_0 \gtrsim \lambda_F$, when the walker dynamics become ballistic. The walker characteristic speed, which may be tuned through the impact phase θ_I, plays an equivalent role: The trajectory of faster droplets is less influenced by the submerged topography, while slower droplets are more susceptible to localization. Finally, observation of walker localization also requires the tile width to be comparable to the Faraday wavelength, $W \sim \lambda_F$. When the tile width is small relative to the Faraday wavelength, $W \ll \lambda_F$, the small-scale features of the topography become imperceptible to the walker, and so its dynamics becomes ballistic. When the tile width is large relative to the Faraday wavelength, $W \gg \lambda_F$, the walker exhibits ballistic motion above the tiles. However, the droplet experiences deflections between the tiles, leading to diffusive motion in the long-time limit. The walker behavior, thus, become similar to that expected for a particle devoid of wavelike characteristics.

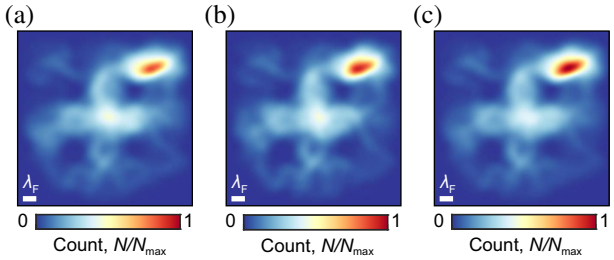

FIG. 15. Ergodicity of the walker localization. Position histogram arising from simulations of the walker model with (a) 36 walker trajectories, each simulated up to 21 000 Faraday periods, (b) one walker trajectory simulated up to 189 000 Faraday periods, and (c) four walker trajectories, each simulated up to 189 000 Faraday periods. In all cases, the emergent position histogram is virtually the same.

j. Numerical convergence

We perform numerical tests to ensure that the spatiotemporal resolution is adequate to render discretization-independent results. Specifically, we repeat the simulations described in Appendix D 1 b with a coarser [$N \times N = 148 \times 148$, $\Delta t = T_F L/(10N\lambda_F)$] and a finer [$N \times N = 408 \times 408$, $\Delta t = T_F L/(20N\lambda_F)$] spatiotemporal discretization to compare the results with the reference case [$N \times N = 204 \times 204$, $\Delta t = T_F L/(10N\lambda_F)$]. The three simulations reveal similar localized statistics (Fig. 16). We, thus, conclude that the intermediate resolution chosen for the reference case is adequate.

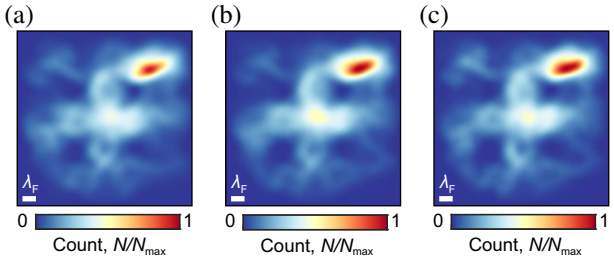

FIG. 16. Numerical discretization of the walker simulations. Position histograms are obtained with different spatiotemporal resolutions, specifically (a) $N \times N = 148 \times 148$ (approximately eight points per tile), (b) 204×204 (approximately 11 points per tile), and (c) 408×408 (approximately 21 points per tile). The temporal resolution is $\Delta t = T_F L/(10N\lambda_F)$ in (a) and (b) and $\Delta t = T_F L/(20N\lambda_F)$ in (c).

2. Waveless particles

To highlight the distinct behavior of the walkers, we compare in Fig. 1 their statistics to those arising from a "waveless" particle, with mass m and average speed v_0, that evolves classically in a random background with the same form as the potential induced by the submerged bottom topography on the walkers. The problem may be nondimensionalized using $x_c = W$, $t_c = W/v_0$, and $V_c = mW^2/v_0^2$ as the characteristic scales for length, time, and energy, respectively, where W is the tile width of the random potential. The dimensionless governing equation for the particle position $\boldsymbol{x}_p(t)$ then becomes

$$\ddot{\boldsymbol{x}}_p(t) = -\nabla V(\boldsymbol{x}_p), \tag{D1}$$

which is initialized at the average speed, i.e., $|\dot{\boldsymbol{x}}_p(0)| = 1$, in a random direction. The initial position is unimportant as long as its associated potential energy is the same as the mean value, thus ensuring that the particle's average speed remains close to unity. Alternatively, we may select the initial position randomly and readjust the initial speed to maintain the same total energy and so obtain the same average speed. We select a potential with the same form as that induced by the walker's bottom topography in the experiments. We, thus, proceed as in Appendix C 2 a and define

$$V(\boldsymbol{x}) = -KH(\boldsymbol{x}), \tag{D2}$$

where, once again, $K = \kappa/V_c$ and $H(\boldsymbol{x})$ have dimensions of 1/length and length, respectively. Here, $H(\boldsymbol{x})$ is the random liquid depth distribution used in the experiments and κ the dimensional scaling constant presented in the main text, which has dimensions of energy/length. We note that subtracting the maximum depth as in Eq. (C6) is not important in this case due to the gradient in Eq. (D1). The rescaling constant K is chosen to ensure the particle energy is greater than the maximum of the potential.

The random region is surrounded by a confining potential (corresponding to the wave damper with double the height about the base depth as in the experiment) to prevent the particle from escaping the domain of interest. The equation of motion is integrated using a fourth-order Runge-Kutta method with adaptive time stepping (MATLAB ode45). We ensure that the numerical tolerances are sufficiently stringent so that the energy of the particles does not vary significantly throughout the simulations, typically remaining within <1% of the initial energy. A low-pass filter of radius (standard deviation) $\sigma = 111\%$ of the lattice frequency is applied to the potential spectrum to prevent diverging gradients between tiles. Tests show that varying the filter radius does not significantly influence the position histogram, where the essential feature is the absence of localization. We match the number of trajectories and their duration to those from experiments and conduct a series of simulations to verify that the particle dynamics converge to the same histogram, regardless of the initial conditions. For the simulations presented in Fig. 1, the potential's rescaling constant is $K = 1.2\ \mathrm{mm}^{-1}$ and the ratio of total energy to maximum potential energy $(\frac{1}{2}|\dot{\boldsymbol{x}}_p|^2 + V)/\max V = 1.32$.

[1] M. C. Marchetti, J. F. Joanny, S. Ramaswamy, T. B. Liverpool, J. Prost, Madan Rao, and R. A. Simha, *Hydrodynamics of soft active matter*, Rev. Mod. Phys. **85**, 1143 (2013).

[2] C. Bechinger, R. Di Leonardo, H. Löwen, C. Reichhardt, G. Volpe, and G. Volpe, *Active particles in complex and crowded environments*, Rev. Mod. Phys. **88**, 045006 (2016).

[3] A. Morin, N. Desreumaux, J-B. Caussin, and D. Bartolo, *Distortion and destruction of colloidal flocks in disordered environments*, Nat. Phys. **13**, 63 (2017).

[4] P. de Anna, A. A. Pahlavan, Y. Yawata, R. Stocker, and R. Juanes, *Chemotaxis under flow disorder shapes microbial dispersion in porous media*, Nat. Phys. **17**, 68 (2021).

[5] M. Z. Hasan and C. L. Kane, *Colloquium: Topological insulators*, Rev. Mod. Phys. **82**, 3045 (2010).

[6] C. Reichhardt, C. J. O. Reichhardt, and M. V. Milošević, *Statics and dynamics of skyrmions interacting with disorder and nanostructures*, Rev. Mod. Phys. **94**, 035005 (2022).

[7] R. Wiesendanger, *Nanoscale magnetic skyrmions in metallic films and multilayers: A new twist for spintronics*, Nat. Rev. Mater. **1**, 1 (2016).

[8] B. Dieny *et al.*, *Opportunities and challenges for spintronics in the microelectronics industry*, National electronics review **3**, 446 (2020).

[9] A. Einstein, *Über einen die erzeugung und verwandlung des lichtes betreffenden heuristischen gesichtspunkt*, Ann. Phys. (Berlin) **322**, 132 (1905).

[10] M. Lévy, P. J. S. Franks, and K. S. Smith, *The role of submesoscale currents in structuring marine ecosystems*, Nat. Commun. **9**, 4758 (2018).

[11] P. W. Anderson, *Absence of diffusion in certain random lattices*, Phys. Rev. **109**, 1492 (1958).

[12] F. Evers and A. D. Mirlin, *Anderson transitions*, Rev. Mod. Phys. **80**, 1355 (2008).
[13] A. Lagendijk, B. Tiggelen, and D. S. Wiersma, *Fifty years of Anderson localization*, Phys. Today **62**, No. 8, 24 (2009).
[14] B. Kramer and. A MacKinnon, *Localization: Theory and experiment*, Rep. Prog. Phys. **56**, 1469 (1993).
[15] M. Imada, A. Fujimori, and Y. Tokura, *Metal-insulator transitions*, Rev. Mod. Phys. **70**, 1039 (1998).
[16] Y. Couder, S. Protière, E. Fort, and A. Boudaoud, *Dynamical phenomena: Walking and orbiting droplets*, Nature (London) **437**, 208 (2005).
[17] See Supplemental Material at http://link.aps.org/supplemental/10.1103/PhysRevX.14.031047 for three supplemental video legends.
[18] J. Billy, V. Josse, Z. Zuo, A. Bernard, B. Hambrecht, P. Lugan, D. Clément, L. Sanchez-Palencia, P. Bouyer, and A Aspect, *Direct observation of Anderson localization of matter waves in a controlled disorder*, Nature (London) **453**, 891 (2008).
[19] G. Roati, C. D'Errico, L. Fallani, M. Fattori, C. Fort, M. Zaccanti, G. Modugno, M. Modugno, and M. Inguscio, *Anderson localization of a non-interacting Bose–Einstein condensate*, Nature (London) **453**, 895 (2008).
[20] F. Jendrzejewski, A. Bernard, K. Müller, P. Cheinet, V. Josse, M. Piraud, L. Pezzé, L. Sanchez-Palencia, A. Aspect, and P. Bouyer, *Three-dimensional localization of ultracold atoms in an optical disordered potential*, Nat. Phys. **8**, 398 (2012).
[21] R. Dalichaouch, J. P. Armstrong, S. Schultz, P. M. Platzman, and S. L. McCall, *Microwave localization by two-dimensional random scattering*, Nature (London) **354**, 53 (1991).
[22] D. S. Wiersma, P. Bartolini, A. Lagendijk, and R. Righini, *Localization of light in a disordered medium*, Nature (London) **390**, 671 (1997).
[23] T. Schwartz, G. Bartal, S. Fishman, and M. Segev, *Transport and Anderson localization in disordered two-dimensional photonic lattices*, Nature (London) **446**, 52 (2007).
[24] M. Segev, Y. Silberberg, and D. N. Christodoulides, *Anderson localization of light*, Nat. Photonics **7**, 197 (2013).
[25] A. Yamilov, S. E. Skipetrov, T. W. Hughes, M. Minkov, Z. Yu, and H. Cao, *Anderson localization of electromagnetic waves in three dimensions*, Nat. Phys. **19**, 1308 (2023).
[26] H. Hu, A. Strybulevych, J. H. Page, S. E. Skipetrov, and B. A. van Tiggelen, *Localization of ultrasound in a three-dimensional elastic network*, Nat. Phys. **4**, 945 (2008).
[27] M. Belzons, E. Guazzelli, and O. Parodi, *Gravity waves on a rough bottom: Experimental evidence of one-dimensional localization*, J. Fluid Mech. **186**, 539 (1988).
[28] P. Devillard, F. Dunlop, and B. Souillard, *Localization of gravity waves on a channel with a random bottom*, J. Fluid Mech. **186**, 521 (1988).
[29] M. Filoche and S. Mayboroda, *Universal mechanism for Anderson and weak localization*, Proc. Natl. Acad. Sci. U.S.A. **109**, 14761 (2012).
[30] J. W. M. Bush and A. U. Oza, *Hydrodynamic quantum analogs*, Rep. Prog. Phys. **84**, 017001 (2021).
[31] S. Protière, A. Boudaoud, and Y. Couder, *Particle-wave association on a fluid interface*, J. Fluid Mech. **554**, 85 (2006).
[32] J. Moláček and J. W. M. Bush, *Drops walking on a vibrating bath: Towards a hydrodynamic pilot-wave theory*, J. Fluid Mech. **727**, 612 (2013).
[33] A. Eddi, E. Sultan, J. Moukhtar, E. Fort, M. Rossi, and Y. Couder, *Information stored in Faraday waves: The origin of a path memory*, J. Fluid Mech. **674**, 433 (2011).
[34] P. J. Sáenz, T. Cristea-Platon, and J. W. M. Bush, *Statistical projection effects in a hydrodynamic pilot-wave system*, Nat. Phys. **14**, 315 (2018).
[35] P. J. Sáenz, T. Cristea-Platon, and J. W. M Bush, *A hydrodynamic analog of Friedel oscillations*, Sci. Adv. **6**, aay9234 (2020).
[36] P. J. Sáenz, G. Pucci, S. E. Turton, A. Goujon, R. R. Rosales, J. Dunkel, and J. W. M. Bush, *Emergent order in hydrodynamic spin lattices*, Nature (London) **596**, 58 (2021).
[37] K. Kumar and L. S. Tuckerman, *Parametric instability of the interface between two fluids*, J. Fluid Mech. **279**, 49 (1994).
[38] L. Tadrist, J.-B. Shim, T. Gilet, and P. Schlagheck, *Faraday instability and subthreshold Faraday waves: Surface waves emitted by walkers*, J. Fluid Mech. **848**, 906 (2018).
[39] C. A. Müller and D. Delande, *Disorder and interference: Localization phenomena*, in *Ultracold Gases and Quantum Information: Lecture Notes of the Les Houches Summer School in Singapore*, Vol. 91, edited by C. Miniatura, L. Kwek, M. Ducloy, B. Grémaud, B.-G. Englert, L. Cugliandolo, A. Ekert, and K. k. Phua (Oxford University, New York, 2011), Chap. 9, pp. 441–533.
[40] E. Fort, A. Eddi, A. Boudaoud, J. Moukhtar, and Y. Couder, *Path-memory induced quantization of classical orbits*, Proc. Natl. Acad. Sci. U.S.A. **107**, 17515 (2010).
[41] A. M. Blitstein, R. R. Rosales, and P. J. Sáenz, *Minimal quantization model in pilot-wave hydrodynamics*, Phys. Rev. Lett. **132**, 104003 (2024).
[42] L. M. Faria, *A model for Faraday pilot waves over variable topography*, J. Fluid Mech. **811**, 51 (2017).
[43] M. Durey, P. A. Milewski, and Z. Wang, *Faraday pilot-wave dynamics in a circular corral*, J. Fluid Mech. **891**, A3 (2020).
[44] M. Durey, P. A. Milewski, and J. W. M. Bush, *Dynamics, emergent statistics, and the mean-pilot-wave potential of walking droplets*, Chaos **28**, 096108 (2018).
[45] C. Jin, C. Krüger, and C. C. Maass, *Chemotaxis and autochemotaxis of self-propelling droplet swimmers*, Proc. Natl. Acad. Sci. U.S.A. **114**, 5089 (2017).
[46] S. Michelin, *Self-propulsion of chemically active droplets*, Annu. Rev. Fluid Mech. **55**, 77 (2023).
[47] P. Le Gal, B. Castillo Morales, S. Hernandez-Zapata, and G. Ruiz Chavarria, *Swimming of a ludion in a stratified sea*, J. Fluid Mech. **931**, A14 (2022).
[48] G. P. Benham, O. Devauchelle, S. W. Morris, and J. A. Neufeld, *Gunwale bobbing*, Phys. Rev. Fluids **7**, 074804 (2022).
[49] I. Ho, G. Pucci, A. U. Oza, and D. M. Harris, *Capillary surfers: Wave-driven particles at a vibrating fluid interface*, Phys. Rev. Fluids **8**, L112001 (2023).
[50] A. Roux, J.-P. Martischang, and M. Baudoin, *Self-radiation force on a moving monopolar source*, J. Fluid Mech. **952**, A22 (2022).

[51] D. N. Arnold, G. David, D. Jerison, S. Mayboroda, and M. Filoche, *Effective confining potential of quantum states in disordered media*, Phys. Rev. Lett. **116**, 056602 (2016).

[52] D. A. Abanin, E. Altman, I. Bloch, and M. Serbyn, *Colloquium: Many-body localization, thermalization, and entanglement*, Rev. Mod. Phys. **91**, 021001 (2019).

[53] J-H Choi, S. Hild, Jo. Zeiher, P. Schauß, A. Rubio-Abadal, T. Yefsah, V. Khemani, D. A Huse, I. Bloch, and C. Gross, *Exploring the many-body localization transition in two dimensions*, Science **352**, 1547 (2016).

[54] E. J. Meier, F. A. An, A. Dauphin, M. Maffei, P. Massignan, T. L. Hughes, and B. Gadway, *Observation of the topological Anderson insulator in disordered atomic wires*, Science **362**, 929 (2018).

[55] S. Shankar, A. Souslov, M. J. Bowick, M. C. Marchetti, and V. Vitelli, *Topological active matter*, Nat. Rev. Phys. **4**, 380 (2022).

[56] S. Douady, *Experimental study of the Faraday instability*, J. Fluid Mech. **221**, 383 (1990).

[57] D. M. Harris and J. W. M. Bush, *Generating uniaxial vibration with an electrodynamic shaker and external air bearing*, J. Sound Vib. **334**, 255 (2015).

[58] J. W. M. Bush, *Pilot-wave hydrodynamics*, Annu. Rev. Fluid Mech. **47**, 269 (2015).

[59] D. M. Harris, T. Liu, and J. W. M. Bush, *A low-cost, precise piezoelectric droplet-on-demand generator*, Exp. Fluids **56**, 1 (2015).

[60] M. Faraday, *On a peculiar class of acoustical figures; and on certain forms assumed by groups of particles upon vibrating elastic surfaces*, Phil. Trans. R. Soc. London **121**, 299 (1831).

[61] P. A. Milewski, C. A. Galeano-Rios, A. Nachbin, and J. W. M. Bush, *Faraday pilot-wave dynamics: Modelling and computation*, J. Fluid Mech. **778**, 361 (2015).

[62] F. Dias, A. I. Dyachenko, and V. E. Zakharov, *Theory of weakly damped free-surface flows: A new formulation based on potential flow solutions*, Phys. Lett. A **372**, 1297 (2008).

[63] M. Durey and P. A. Milewski, *Faraday wave-droplet dynamics: Discrete-time analysis*, J. Fluid Mech. **821**, 296 (2017).

[64] K. Kumar, *Linear theory of Faraday instability in viscous fluids*, Proc. R. Soc. A **452**, 1113 (1996).

[65] M. Durey, *Faraday wave-droplet dynamics: A hydrodynamic quantum analogue*, Ph.D. thesis, University of Bath, 2018.

[66] A. Nachbin, P. A. Milewski, and J. W. M. Bush, *Tunneling with a hydrodynamic pilot-wave model*, Phys. Rev. Fluids **2**, 034801 (2017).

[67] E. Abrahams, P. W. Anderson, D. C. Licciardello, and T. V. Ramakrishnan, *Scaling theory of localization: Absence of quantum diffusion in two dimensions*, Phys. Rev. Lett. **42**, 673 (1979).

[68] T. Cristea-platon, P. J. Sáenz, and J. W. M. Bush, *Walking droplets in a circular corral: Quantisation and chaos*, Chaos **28**, 096116 (2018).